minerals

MDPI

Article

Multiple Stage Ore Formation in the Chadormalu Iron Deposit, Bafq Metallogenic Province, Central Iran: Evidence from BSE Imaging and Apatite EPMA and LA-ICP-MS U-Pb Geochronology

Hassan Heidarian [1,*], David R. Lentz [1], Saeed Alirezaei [2], Christopher R. M. McFarlane [1] and Sima Peighambari [3]

[1] Department of Earth Sciences, University of New Brunswick, Fredericton, NB E3B 5A3, Canada; dlentz@unb.ca (D.R.L.); crmm@unb.ca (C.R.M.M.)
[2] Faculty of Earth Sciences, Shahid Beheshti University, Evin, P.O. Box 1983969411, Tehran, Iran; S-Alirezaei@sbu.ac.ir
[3] Department of Geology, Payame Noor University, P.O. Box 193953697, Tehran, Iran; Peighambari@pnu.ac.ir
* Correspondence: Ha.Heidarian@unb.ca; Tel.: +1-506-447-3190

Received: 29 September 2017; Accepted: 23 February 2018; Published: 27 February 2018

Abstract: The Chadormalu magnetite-apatite deposit in Bafq metallogenic province, Central Iran, is hosted in the late Precambrian-lower Cambrian volcano-sedimentary rocks with sodic, calcic, and potassic alterations characteristic of iron oxide copper-gold (IOCG) and iron oxide-apatite (IOA) ore systems. Apatite occurs as scattered irregular veinlets and disseminated grains, respectively, within and in the marginal parts of the main ore-body, as well as apatite-magnetite veins in altered wall rocks. Textural evidence (SEM-BSE images) of these apatites shows primary bright, and secondary dark areas with inclusions of monazite/xenotime. The primary, monazite-free fluorapatite contains higher concentrations of Na, Si, S, and light rare earth elements (LREE). The apatite was altered by hydrothermal events that led to leaching of Na, Si, and REE + Y, and development of the dark apatite. The bright apatite yielded two U-Pb age populations, an older dominant age of 490 ± 21 Ma, similar to other iron deposits in the Bafq district and associated intrusions, and a younger age of 246 ± 17 Ma. The dark apatite yielded a U-Pb age of 437 ± 12 Ma. Our data suggest that hydrothermal magmatic fluids contributed to formation of the primary fluorapatite, and sodic and calcic alterations. The primary apatite reequilibrated with basinal brines in at least two regional extensions and basin developments in Silurian and Triassic in Central Iran.

Keywords: Chadormalu; Kiruna-type; iron oxide-apatite; U-Pb geochronology; Bafq; Iran

1. Introduction

The formation of apatite-bearing iron deposits is a current topic of debate. The deposits are characterized by large masses of Ti-rich to Ti-poor Fe oxides (essentially magnetite) and subordinate phosphates, in particular apatite, and are known as Kiruna-type magnetite-apatite (e.g., [1]) or iron oxide-apatite (IOA) deposits [2]. Some researchers (e.g., [3–6] included the Kiruna-type apatite-bearing Fe-oxide deposits in the wide range of the iron oxide copper-gold (IOCG) deposits. However, the deposits are considered by other researchers (e.g., [7,8]) as a distinct type of iron deposits, known as iron oxide-apatite (IOA) ores.

Apatite is a common accessory mineral in a wide range of magmatic, sedimentary, and metamorphic rocks. Apatites can serve as a useful indicator mineral for IOCG- and IOA-type

deposits, recording the origin and nature of the associated host rocks and the volatile contents of the ore fluids (e.g., [9–11]). Apatite is known to accommodate significant amounts of Y + REE, Si, and Na [12]. The composition and crystal structure of apatite favors substitution of light rare earth elements (LREE).

Experimental studies on apatite indicate that the mineral can be chemically altered through interaction with aqueous brines, pure H_2O, and acidic aqueous fluids over a wide range of temperatures and pressures (300–900 °C and 0.5–1.0 GPa) [13]. Alteration of apatite may lead to the formation of monazite [(Ce, LREE) PO_4] and/or xenotime [(Y, HREE) PO_4] occurring as inclusions in apatite or as discrete grains on the surface of the mineral (e.g., [14,15]). Monazite and xenotime inclusions typically nucleate as a product of fluid-induced multi-elements redistribution within apatite (e.g., [15,16]).

Apatite can serve as a fingerprint for metasomatic reactions, and provides information on the temperature, composition, and nature of the fluids, as well as timing and duration of metasomatic processes [13]. Apatite chemistry can be used as a tool to investigate the nature of fluids involved in alteration-mineralization and development of REE-enriched apatite in IOA deposits. Precise characterization and dating of various apatite generations is important to unraveling the history of ore formation in apatite-bearing ore deposits, such as Kiruna-type iron ores.

The Bafq metallogenic district in Central Iran is a major host to IOA deposits, including the world-class Chadormalu (e.g., [17–22]). Here, we present data on the geochemistry and geochronology of apatite from the Chadormalu and discuss the data in the context of the origin and evolution of ore fluids and ore-forming processes.

2. Geological Setting

2.1. Regional Geology

The Bafq mining district lies in the Posht-e-Badam block [23,24] or Kashmar-Kerman belt [25] in Central Iran (Figure 1). The district is distinguished by a Neoproterozoic basement of Gondwanan affinity consisting of various schists, gneisses, and granitic gneisses covered by the late Precambrian-Triassic rocks [23,26–28]. The late Precambrian cover rocks consist of phyllite, slate, quartzite, and mafic volcanic rocks of the Tashk Formation [20]. The metamorphic assemblage is covered by non-metamorphosed (or slightly metamorphosed) terrestrial to shallow marine rocks containing Ediacaran fauna [29] associated with a bimodal volcanic unit [27]. Rhyolitic and dacitic lava flows and tuffs associated with subordinate andesite, spilitic basalt, and rare nephelinitic to basanitic lava flows are the main volcanic products in the district. The rocks, divided into five members under the Late Precambrian (Vendian) Saghand volcano-sedimentary Formation [30], host the majority of IOA, Pb-Zn, and U ore deposits in Central Iran (Figure 2 in [31]). The sedimentary rocks consist of basal conglomerate, sandstones, shales, dolomites, dolomitic limestones, and evaporites. The upper shale, carbonate, and evaporites, with minor intercalated felsic and mafic volcanic rocks have been introduced as Rizu and Desu series by Huckriede et al. (1962) [32] elsewhere in Central Iran. Borumandi (1973) [26] proposed the term "Esfordi Formation" for this series in the Bafq region. Ramezani and Tucker (2003) [25] assigned a dominantly Early Cambrian age (529–554 Ma) for the volcanic components of this volcano-sedimentary series and referred to that as the CVSU (Cambrian Volcano Sedimentary Unit). The iron deposits in the Bafq district are mostly hosted in metasomatized CVSU and shallow intermediate to felsic intrusions.

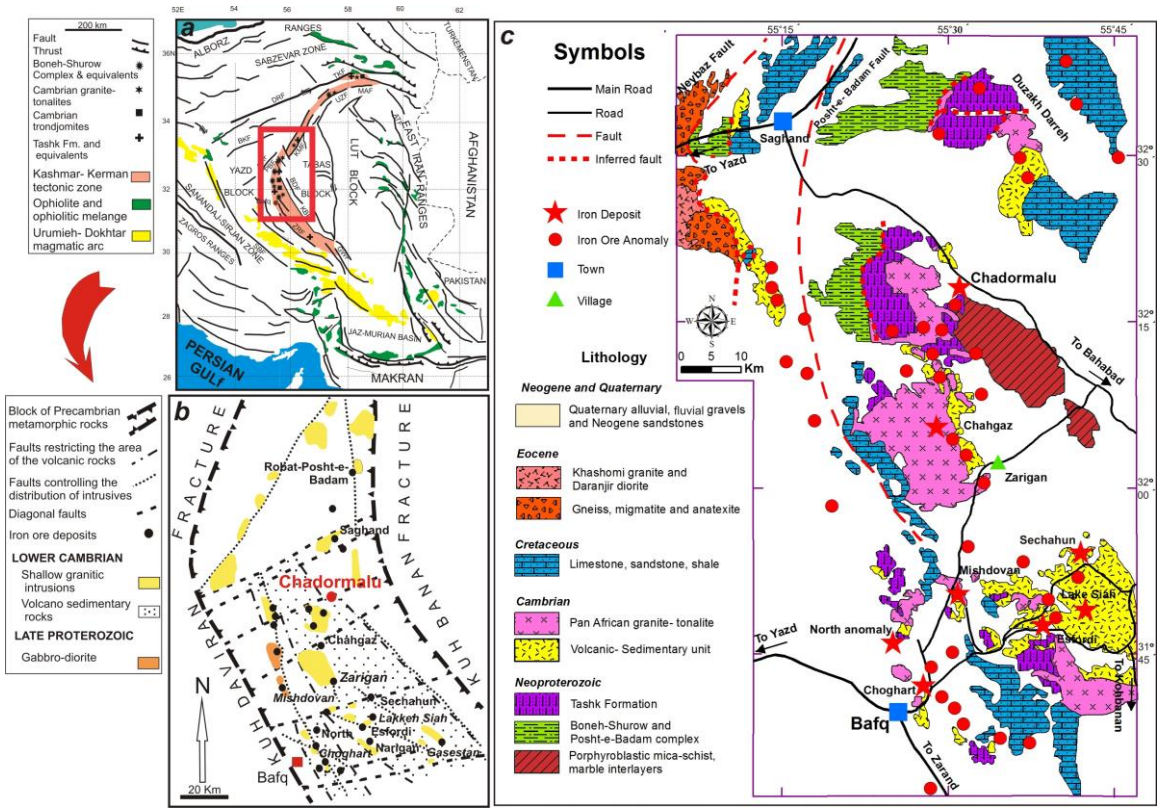

Figure 1. (**a**,**b**) Distribution of iron oxide-apatite deposits in the Kashmar-Kerman volcano-plutonic belt (modified after [19]); (**c**) Geological map of the Posht-e-Badam area (modified after [24,28,33]).

2.2. Previous Geochronology

The Bafq district iron oxide ores are locally associated with REE-rich apatite ± silicate ± carbonate assemblages [34]. The timing of ore formation at Choghart has been constrained to be 515 ± 21 Ma and 529 ± 21 Ma (monazite Th-U-Pb total method; [35]). Using isotopic U-Pb dating, Stosch et al. (2011) [34] reported a range of 527 to 539 Ma for apatite samples from five iron deposits in the Bafq district. These ages fall in the age range for felsic plutonic and volcanic rocks in the district (525–545 Ma, zircon U-Pb; [25]). However, Bonyadi et al. (2011) [36] reported a U-Pb LA-ICP-MS age of 510 ± 8 Ma for REE-rich fluorapatite and the associated semi-massive magnetite from the Se-Chahun complex in the Bafq district. The authors reported a slightly older U-Pb age (525 ± 7 Ma) for sodic alteration from the same deposit.

2.3. Mine-Scale Geology

The Chadormalu deposit consists of two separate large massive ore bodies (Figure 2). The main orebody, consisting of three closely spaced bodies in the northern part of the deposit, accounts for about 80% of the total ore reserve. Smaller ore bodies displaying faulted and brecciated contacts with metasomatized greenish host rocks occur in the southern part of the deposit. Apatite is a common accessory mineral. Magnetite also occurs in magnetite-apatite veins with sharp contacts against the altered host rocks. The veins locally contain fragments of host rocks and display a brecciated appearance. Minor hematite, ankerite, and siderite locally occur associated with magnetite from Chadormalu.

The field relationships in the Chadormalu deposit are documented by Heidarian et al. [31]. Intense alteration has obscured the original mineralogy and texture of the host rocks. Sodic alteration, marked by replacive albitization of the various original minerals is widespread and occurs as a distal feature in Chadormalu. Calcic or calcic-ferroan alteration, distinguished by the development of variable proportions of actinolite replacing various rocks, including the albitized rocks, occurs as a more proximal feature, increasing in intensity towards the ore bodies. A potassic alteration, marked

by the development of K-feldspar, sericite, and biotite, locally occurs in the host rocks and appears to be post-dating earlier sodic and calcic alteration assemblages. Two other alteration types are silicification and carbonatization formed during and after the sodic and calcic-ferroan alteration types [19,31,37,38]. Minor chlorite locally occurs in the immediate wall rocks enclosing the vein-type ores. The various alteration types and their relationships in Chadormalu are schematically shown in Figure 2. During the waning stages of magnetite mineralization, minor sulfide minerals, mostly pyrite, developed as irregular veinlets and interstitial grains.

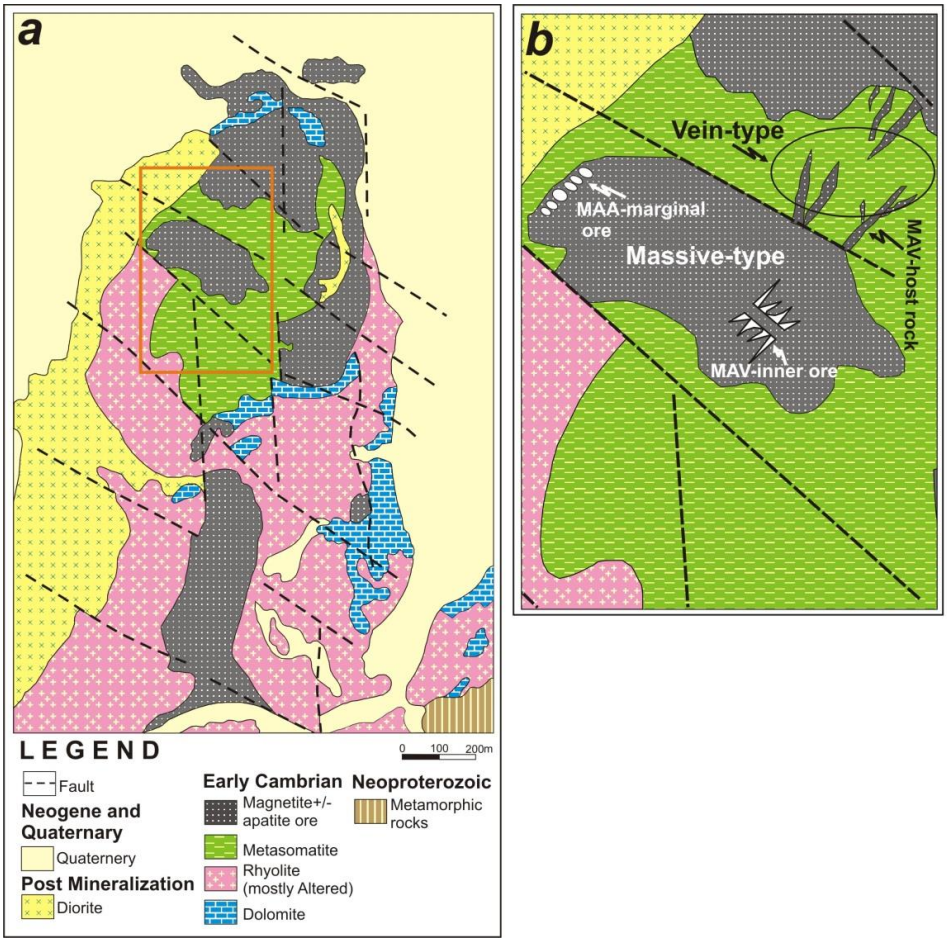

Figure 2. (**a**) Simplified geological map schematically showing the alteration types and their relationships in the Chadormalu deposit (modified from [39,40]). (**b**) Enlarged view of the square in (a) to show details of the ore types (this study). Magnetite-apatite veins in altered host rocks (MAV-host rock); Disseminated magnetite-apatite associations in the marginal parts of the main ore body (MAA-marginal ore); Magnetite-apatite veinlets in the internal parts of the main magnetite ore body (MAV-inner ore).

The ore texture/structure, wall rock alteration, and the common occurrence of apatite in the Chadormalu, and most other iron oxide deposits in the Bafq district (e.g., [19,31,41]) are consistent with their classification as IOA deposits. Apatite in Chadormalu occurs as magnetite-apatite veins cutting the altered rocks (Figure 3a,b); as disseminated magnetite-apatite associations and grain aggregates in the marginal parts of the main ore body (Figure 3c,d); and as irregular magnetite-apatite veinlets in the internal parts of the main ore body (Figure 3e,f).

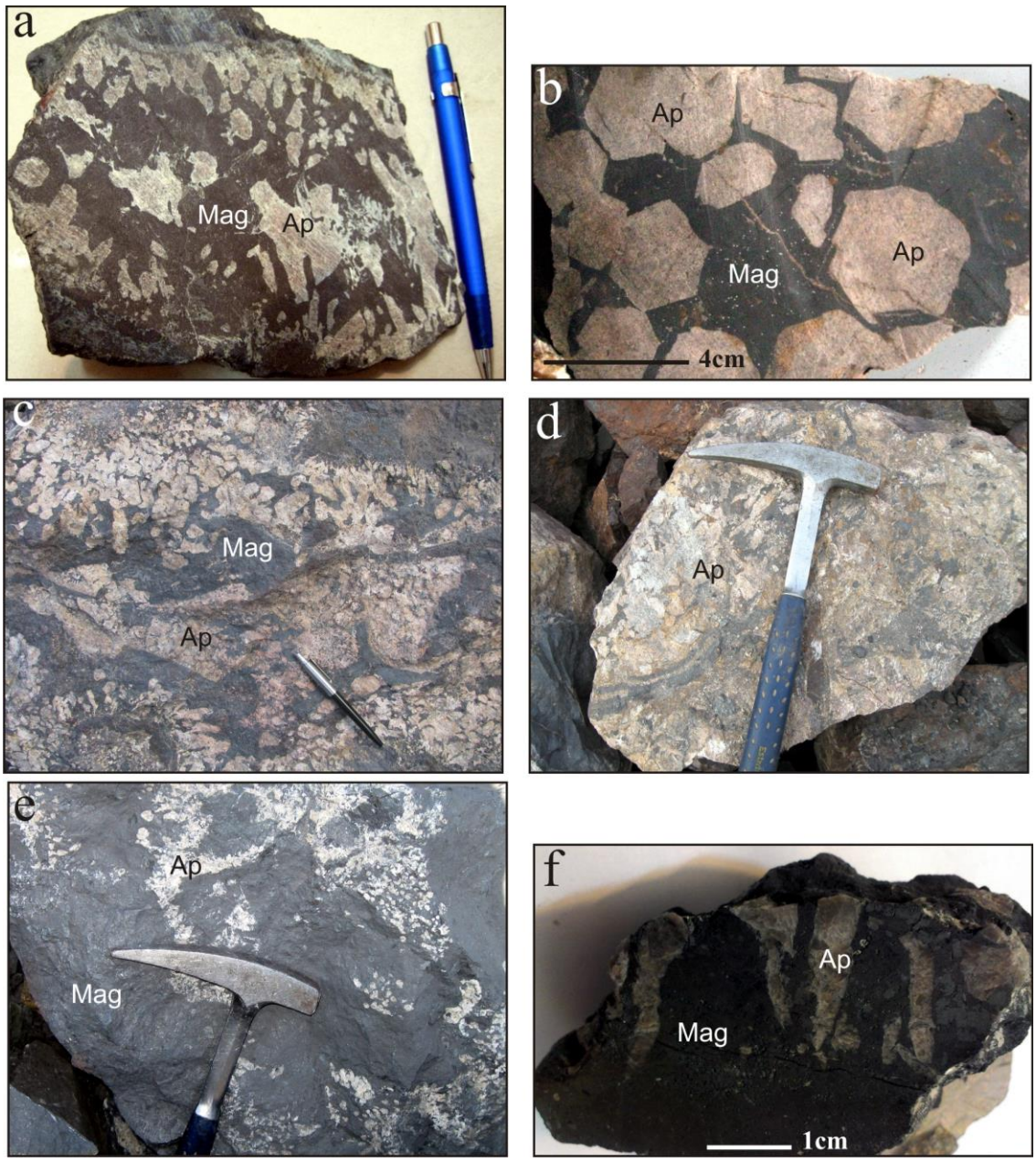

Figure 3. Photographs of representative samples from the main apatite-magnetite associations in Chadormalu. (**a**,**b**) Magnetite-apatite association from veins in the altered host rocks. (**c**) Apatite grains and grain aggregates in the marginal part of the main ore body. (**d**) Brecciated apatite and associated magnetite in the marginal parts of the main ore body. (**e**,**f**) Irregular apatite veinlets and streaks in the main ore body. Abbreviations: Ap = apatite; Mag = magnetite.

3. Materials and Methods

In this study, 8 samples representing various types of apatite associated with iron ores were selected for petrography, scanning electron microscopy using backscatter electron detector (SEM-BSE), electron probe microanalysis (EPMA), and laser ablation-inductively coupled plasma-mass spectrometry (LA-ICP-MS). The samples include four (Cha2-1, Cha2-2, Cha8, Ch15) from magnetite-apatite veins in the altered host rocks (MAV-host rock type), two (Cha1-1, Cha1-2) from disseminated apatite grains and grain aggregates in the marginal parts of the main ore body (MAA-marginal type), and two (Cha24-1, Cha24-2) from magnetite-apatite veinlets in the internal parts of the main magnetite ore body (MAV-inner ore type) (Figure 3). A schematic map illustrating the location of the three types of apatite is shown in Figure 2b. A description of the samples is presented in Table 1 and the locations of the samples are shown in Figure 4.

Table 1. Classification of the samples representing three different apatite types and their locations, in the Chadormalu deposit.

Type	Samples	Description	Location
MAV-host rock	Cha2-1, Cha2-2, Cha8, Ch15	Magnetite-apatite veins showing typical comb-like textures	Greenish altered host rocks
MAA-marginal	Cha1-1, Cha1-2	Euhedral to anhedral apatite grains and grain aggregates	Marginal parts of the main ore body
MAV-inner ore	Cha24-1, Cha24-2	Irregular veins and veinlets, as well as scattered apatite grains	Internal parts of the main ore body

The various apatite types were studied using a dPict32 (Geller MicroAnalytical Laboratory Inc., Topsfield, MA, USA) for SEM-BSE images. The apatite types were analyzed using a JEOL JXA-733 Superprobe Microanalyzer (Peabody, MA, USA), equipped with four two-crystal wavelength-dispersive spectrometers at the University of New Brunswick (UNB), Fredericton, NB, Canada. The analyses were performed under an accelerating voltage of 15 kV and a probe current of 30 nA. The following reference minerals were used: $NaAlSi_2O_6$·(Na), Mg_2SiO_4·(Mg), $(Ca,Na)Al_2Si_2O_8$·(Al), $Mg_3Al_2Si_3O_{12}$·(Si), $Ca_5(PO_4)_3(OH,F,Cl)$·(P and Ca), $BaSO_4$·(S and Ba), $KAlSi_3O_8$·(K), vanadium metal (V), $CaMnSi_2O_6$·(Mn), Fe_2O_3·(Fe), $SrSO_4$·(Sr), $Y_2CaMg_2(SiO_4)_3$, $CePO_4$·(Ce), thorium metal (Th), uranium metal (U), $Ca_2MgFeSi_8O_{22}(OH,F)_2$, and $Na_4AlBeSiO_4Cl_{12}$. Detection limits are: 0.038 wt % for P_2O_5, 0.011 wt % for SiO_2, 0.011 wt % for Al_2O_3, 0.034 wt % for SO_3, 0.035 wt % for Y_2O_3, 0.119 wt % for Ce_2O_3, 0.115 wt % for ThO_2, 0.103 wt % for UO_2, 0.01 wt % for MgO, 0.022 wt % for CaO, 0.022 wt % for V_2O_5, 0.037 wt % for MnO, 0.045 wt % for FeO, 0.024 wt % for SrO, 0.037 wt % for BaO, 0.02 wt % for Na_2O, 0.014 wt % for K_2O, 0.022 wt % for F, and 0.013 wt % for Cl.

In situ fluorapatite trace-element analyses were obtained for the same areas analyzed by EPMA with an Australian Scientific Instrument M-50 193 nm ArF (excimer) laser ablation system featuring a Laurin Technic Pty. S-155 large-format cell. The cell is coupled, via Nylon™ tubing, with an Agilent 7700x quadrupole ICP-MS at the Department of Earth Sciences, University of New Brunswick. Operating conditions for apatite U-Pb geochronology are explained in [42]. Trace-element concentrations were normalized to NIST610 as external standard; NIST612 was used as a consistency standard and an estimated Ca content of 39 wt % in apatite was used as internal standard. Minimum detection limits for Y and REE analyzed by LA-ICP-MS are <0.5 ppm and <0.05 ppm for Pb, Th, and U.

The element list was extended to include ^{204}Pb, ^{206}Pb, ^{207}Pb, and ^{238}U (^{235}U calculated assuming $^{238}U/^{235}U = 137.88$) so that a U-Pb age could be obtained for distinct compositional domains. The MAD apatite standard [43] was used as a primary standard for U-Pb geochronology, and an in-house Phalaborwa apatite (~2030 Ma) was used to check the accuracy of calculated ages. The measured age for Phalaborwa of 2031 ± 43 Ma (n = 12; MSWD = 0.42) confirms the overall accuracy of the U-Pb apatite ages for Chadormalu. For both trace-element and U-Pb dating off-line selection and integration of background and analyzed signals, and time-drift correction and quantitative calibration for U-Pb dating and trace element concentrations were performed with Iolite 3.5 using the VizualAge_UcomPbine [44] and trace-element (Internally Standardized) data reduction schemes, respectively. Details of the error propagation are given in Paton (2010) [45]. The Tera-Wasserburg diagrams and lower intercept age calculations were obtained using Isoplot/Ex_ver3.75 [46].

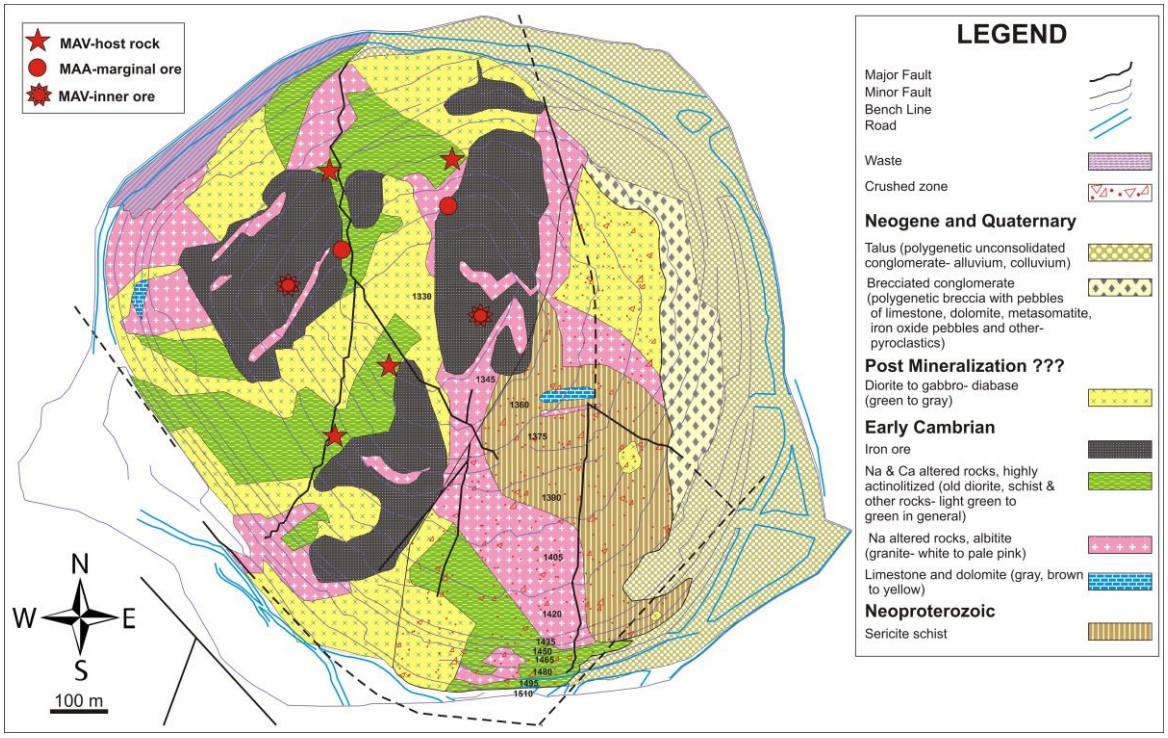

Figure 4. Geological map of the Chadormalu deposit [47] showing the locations of the samples representing the three main apatite types selected for this study.

4. Results

In this study, we have focused on the characteristics of the three main apatite types, including aspects of texture, mineralogy, geochemistry, and geochronology with the aim to investigate and better understand the source and evolution of the ore fluids and the timing of ore formation and any modifications to the ores after original deposition.

4.1. Microtextures

4.1.1. MAV-Host Rock Type

Apatites occurring in magnetite-apatite veins in the greenish altered wall rocks display typical comb-like textures with elongated crystals growing from the walls inward (Figure 3a,b). Similar textures have been reported from several other IOA type deposits in the Bafq district, including Se-Chahun (cf. [36]) and Gazestan [48], from Chilean IOA deposits [49], and from Yangtze Valley Mesozoic IOCG-IOA deposits, China [42]. Apatite also occurs as euhedral crystals enclosed in magnetite in the central parts of the veins (Figure 5b). Minor hematite, pyrite, quartz, and actinolite occur in the apatite-magnetite veins.

High-resolution SEM images on this apatite type reflect common dark patches overprinting the SEM-bright apatite (Figure 5a,c). No preferred orientation or pattern is displayed by the dark areas. The dark areas locally contain inclusions of monazite and less commonly xenotime (Figure 5b,c). The bright areas in the sample Ch15 were found to contain inclusions of allanite typically occurring along fractures (Figure 5d).

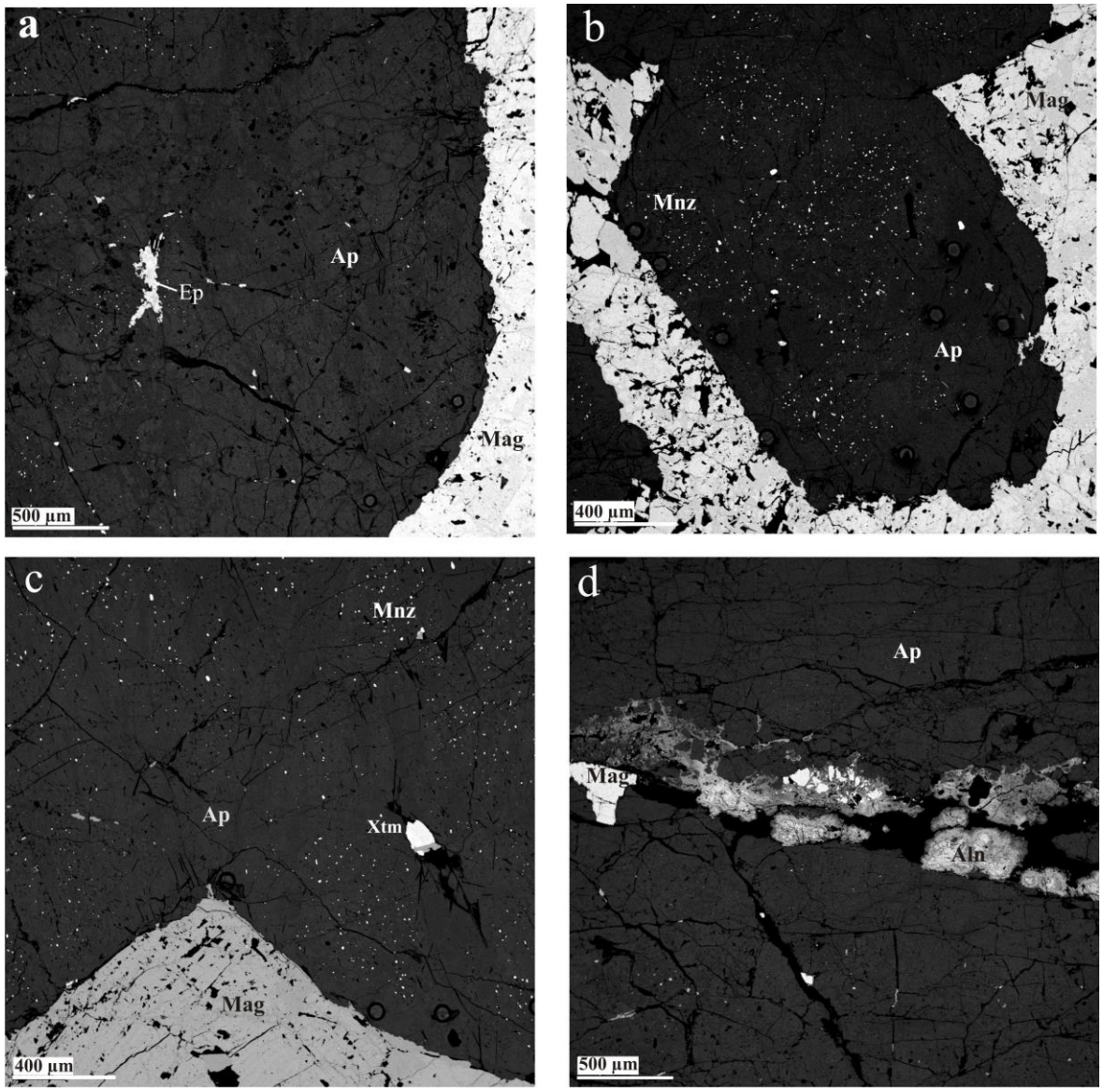

Figure 5. SEM-BSE images of apatite from MAV-host rocks in the Chadormalu iron ores. (**a**) Irregular dark and bright areas in apatites; (**b**) Euhedral apatites with monazite inclusions. Larger monazite grains might have been formed due to an Ostwald ripening like process; (**c**) Fine monazite and a large xenotime inclusions (bright) dispersed in the apatite; (**d**) Magnetite and allanite crystals situated along a crack in apatite. Abbreviations: Ap = apatite; Mag = magnetite; Mnz = monazite; Xtm = xenotime; Aln = allanite; Ep = epidote.

4.1.2. MAA-Marginal Type

This type of apatite consists of euhedral to anhedral apatite grains and grain aggregates in the marginal parts of the main ore body. The apatite and the associated magnetite are locally brecciated and cemented by calcite (Figure 6a,b). Minor hematite, quartz, and pyrite can also be distinguished. On SEM images, this apatite type has dark patches that encroach on the bright parts, similar to the apatite veins in the altered host rocks (Figure 6c,d). Scattered monazite inclusions occur in the dark areas (Figure 6d). Monazite also occurs along apatite grain boundaries (Figure 6c).

4.1.3. MAV-Inner Type

This apatite type occurs as irregular veins and veinlets, as well as scattered apatite grains in the internal parts of the main ore body. The apatite crystals locally show a banded structure marked by alternating apatite- and magnetite-rich bands with relatively constant thickness (Figure 7a). Magnetite has also been formed as euhedral small grains in the fractures and enveloping the primary apatites (Figure 7b). Minor quartz, calcite, hematite, and sulfide occur in this type of apatite-bearing iron ore. On high resolution SEM images, abundant fine-grained monazite inclusions are evident as well as along fractures (Figure 7c,d). The SEM images show dark and bright patches in this type of apatite (Figure 7c), with the dark parts commonly occurring along fractures. Monazite grains are more abundant in the dark areas. The monazite inclusions locally display lower abundance, but coarser crystal sizes in the apatite (Figure 7b).

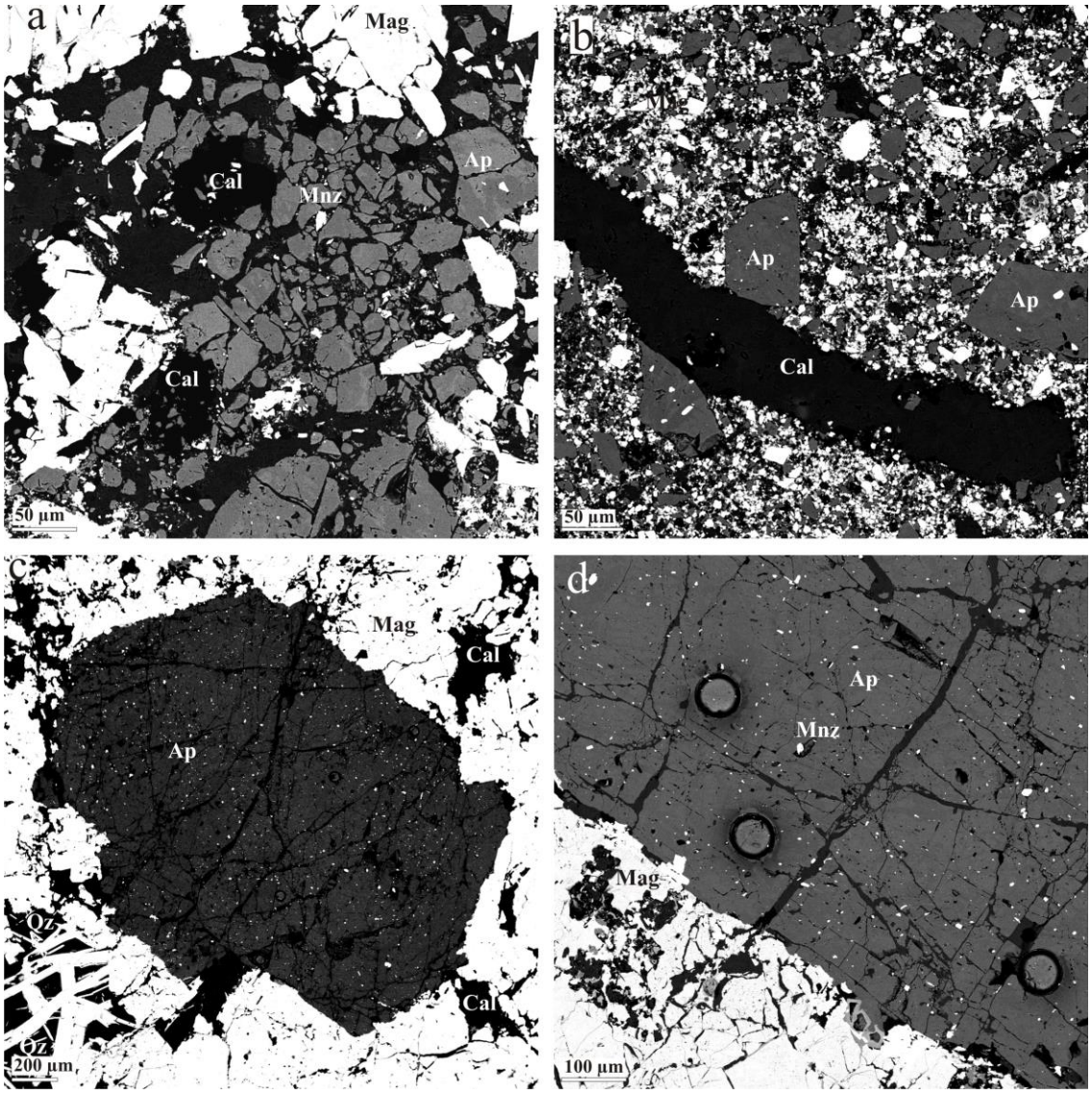

Figure 6. SEM-BSE images of apatite from MAA-marginal type in the Chadormalu iron ores. (**a**,**b**) Brecciated apatite (gray) and magnetite (white) crystals. In details, the apatites show dark and bright zones with fine monazite inclusions; (**c**) Euhedral apatite crystals (medium gray) with monazite grains (bright spots) enclosed in magnetite-hematite (light grey); (**d**) Apatite (grey) with fine monazite inclusions (bright spots within Ap) mostly near or on the fractures, enclosed in magnetite (light grey, lower left). Abbreviations: Ap = apatite; Mag = magnetite; Mnz = monazite; Cal = calcite; Qz = quartz.

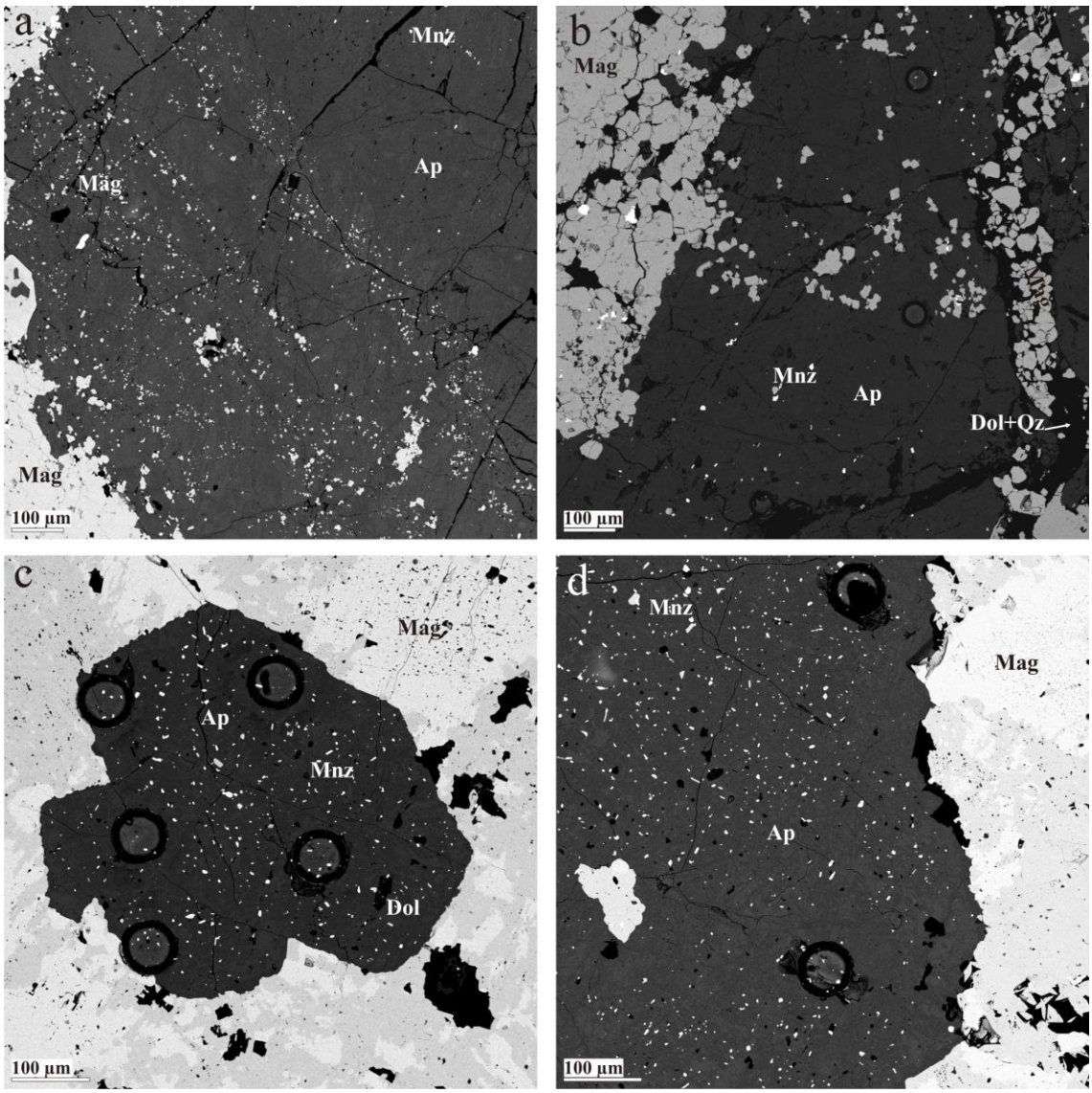

Figure 7. SEM-BSE images of apatite from MAV-inner type in the Chadormalu iron ores. (**a**) Banded structure with magnetite-rich bands in the marginal part of a coarse apatite crystal showing bright and dark areas; (**b**) Euhedral magnetite crystals in the host apatite; (**c**) Euhedral apatite crystals with abundant fine to coarser monazite inclusions; (**d**) Apatite (medium gray) with abundant fine monazite (bright) inclusions associated with magnetite (light grey). Abbreviations: Ap = apatite; Mag = magnetite; Mnz = monazite; Dol = dolomite; Qz = quartz.

4.2. Mineral Composition

4.2.1. Electron Probe Microanalysis (EPMA)

Eight samples from three different apatite types discussed above were selected for EPMA and SEM studies (Tables 2–4). Figure 8 shows comparative box-plot diagrams for selected oxides for various apatite types. The OH values were calculated via charge balance on the halogen site, following Piccoli and Candela [50]. Figure 9 shows a ternary diagram for the composition of the SEM bright and dark areas in the various apatite types in terms of F-OH-Cl contents. The diagram reveals that Chadormalu apatites are mostly fluorapatite. Similar apatite compositions have been reported for several other magnetite-apatite deposits from the Bafq district, such as Esfordi [18,35,36,51,52]. The significantly higher F contents, compared to Cl, as documented for Chadormalu, seems to be a characteristic feature of other IOA type deposits like the Kirunavaara deposit in north Sweden [53].

According to the SEM images and EPMA from different apatite types, the bright apatites contain more Cl compared to the dark apatites. The Na_2O, SiO_2, FeO, and SO_3 in bright parts are significantly

higher than those in the dark areas. Of the REE, only Ce was systematically detected in both dark and bright areas, where Ce in dark spots was found to be generally lower than that in the bright spots.

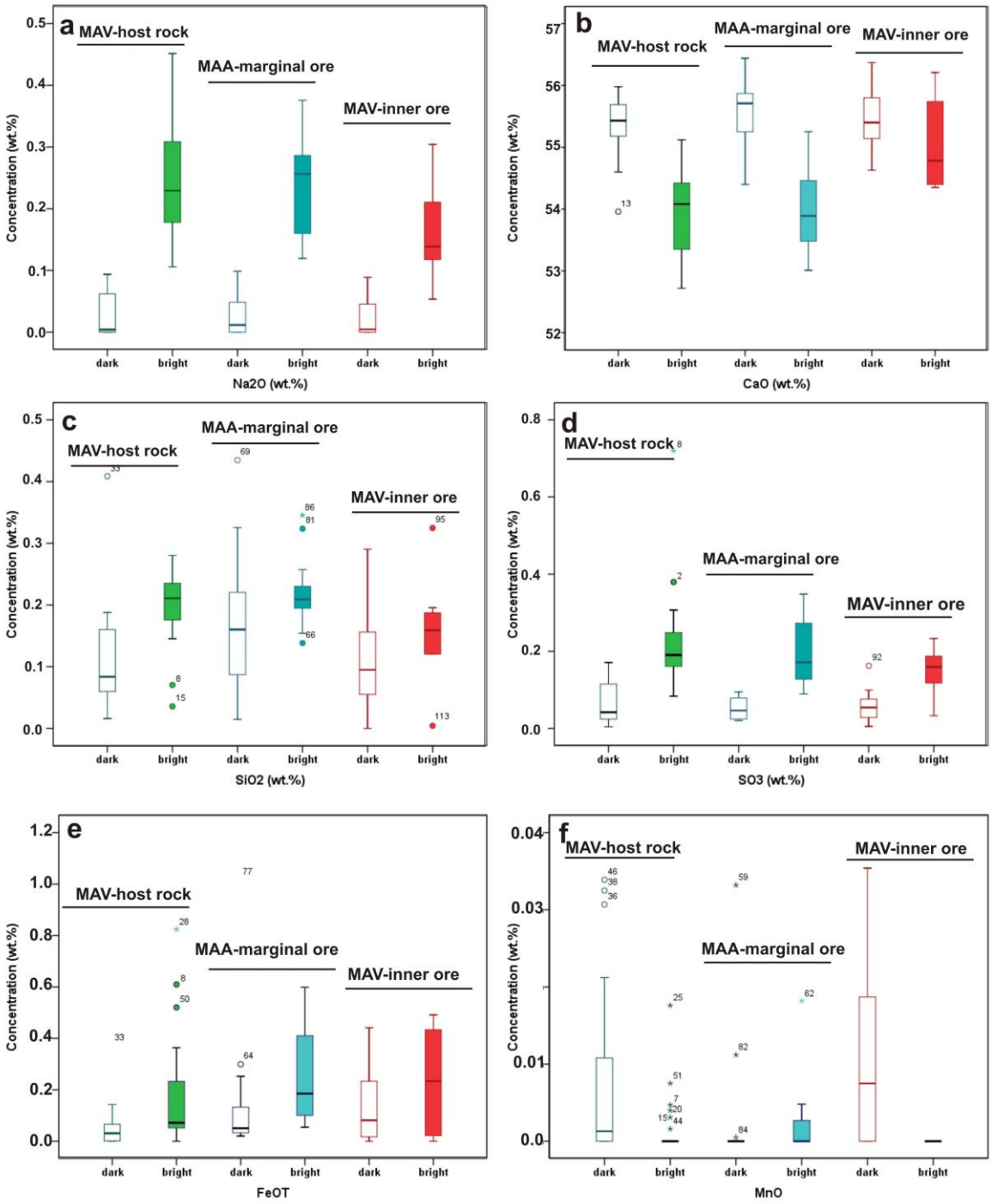

Figure 8. (**a**–**f**) Comparative box-plots for selected key oxides for various apatite types from the Chadormalu iron deposit.

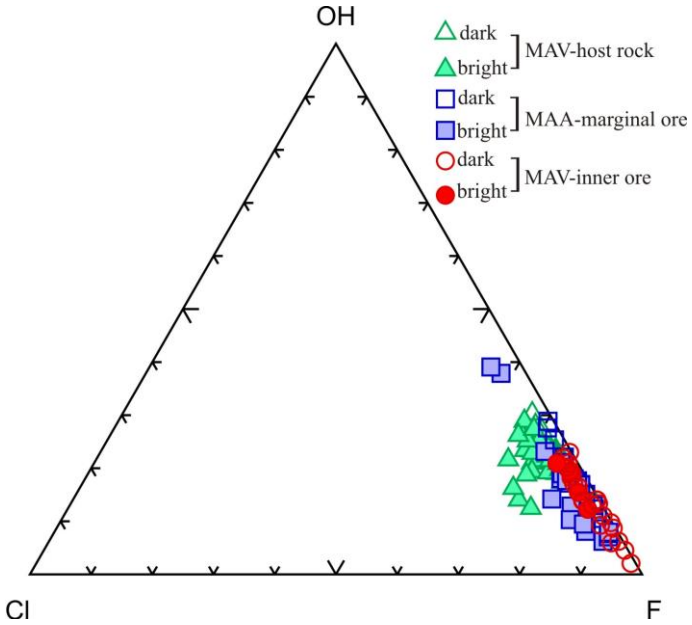

Figure 9. Ternary plot for bright and dark apatite areas from different apatite types from the Chadormalu ores and host rocks in terms of F-OH-Cl atomic proportions.

Table 2. EPMA data (wt %) for bright and dark apatites from Chadormalu MAV-host rock apatite type.

Oxide wt %	Apatite			
	Bright (n = 30)		Dark (n = 24)	
	Mean	SD	Mean	SD
Na_2O	0.25	0.10	0.03	0.03
MgO	0.05	0.02	0.02	0.03
Al_2O_3	0.01	0.01	0.01	0.01
SiO_2	0.20	0.05	0.11	0.08
P_2O_5	41.22	0.68	41.60	0.95
SO_3	0.22	0.12	0.07	0.05
K_2O	mdl	mdl	mdl	mdl
CaO	53.93	0.66	55.39	0.46
V_2O_5	0.01	0.01	0.01	0.01
MnO	mdl	mdl	0.01	0.01
FeO	0.17	0.20	0.05	0.08
SrO	0.02	0.01	0.01	0.01
Y_2O_3	0.11	0.03	0.05	0.04
BaO	mdl	mdl	0.01	0.01
Ce_2O_3	0.73	0.21	0.16	0.12
ThO_2	mdl	mdl	0.01	0.04
UO_2	0.01	0.02	0.01	0.01
F	1.44	0.06	1.51	0.07
Cl	0.13	0.06	0.05	0.01
OH	0.44	0.08	0.44	0.07
Total	98.77	0.89	99.31	0.84

mdl = Minimum detection limit, SD = Standard deviation.

Table 3. EPMA data (wt %) for bright and dark apatites from Chadormalu MAA-marginal ore apatite type.

Oxide wt %	Apatite			
	Bright (n = 17)		Dark (n = 17)	
	Mean	SD	Mean	SD
Na_2O	0.23	0.08	0.03	0.03
MgO	0.05	0.01	0.01	0.01
Al_2O_3	0.04	0.09	0.01	0.02
SiO_2	0.22	0.05	0.18	0.11
P_2O_5	41.60	0.72	42.09	0.46
SO_3	0.20	0.09	0.05	0.03
K_2O	mdl	mdl	mdl	mdl
CaO	53.98	0.67	55.58	0.60
V_2O_5	0.01	0.01	0.01	0.01
MnO	mdl	0.01	mdl	0.01
FeO	0.24	0.17	0.14	0.24
SrO	0.02	0.01	0.01	0.01
Y_2O_3	0.09	0.02	0.08	0.05
BaO	mdl	mdl	mdl	0.01
Ce_2O_3	0.69	0.16	0.20	0.11
ThO_2	0.03	0.06	0.02	0.05
UO_2	0.01	0.02	0.01	0.01
F	1.57	0.19	1.68	0.18
Cl	0.08	0.03	0.04	0.01
OH	0.35	0.19	0.28	0.18
Total	99.31	0.92	100.34	0.67

mdl = Minimum detection limit, SD = Standard deviation.

Table 4. EPMA data (wt %) for bright and dark apatites from Chadormalu MAV-inner ore apatite type.

Oxide (wt %)	Apatite			
	Bright (n = 10)		Dark (n = 20)	
	Mean	SD	Mean	SD
Na_2O	0.17	0.08	0.17	0.08
MgO	0.03	0.01	0.03	0.01
Al_2O_3	0.04	0.12	0.04	0.12
SiO_2	0.16	0.08	0.16	0.08
P_2O_5	41.70	0.38	41.70	0.38
SO_3	0.15	0.06	0.15	0.06
K_2O	mdl	mdl	mdl	mdl
CaO	55.07	0.74	55.07	0.74
V_2O_5	0.01	0.01	0.01	0.01
MnO	mdl	mdl	mdl	mdl
FeO	0.23	0.21	0.23	0.21
SrO	0.03	0.02	0.03	0.02
Y_2O_3	0.07	0.04	0.07	0.04
BaO	mdl	mdl	mdl	mdl
Ce_2O_3	0.48	0.21	0.48	0.21
ThO_2	0.03	0.08	0.03	0.08
UO_2	0.01	0.01	0.01	0.01
F	1.77	0.17	1.77	0.17
Cl	0.03	0.02	0.03	0.02
OH	0.20	0.16	0.20	0.16
Total	100.16	0.52	100.16	0.52

mdl = Minimum detection limit, SD = Standard deviation.

In the MAV-host rock apatites, the Na_2O and SiO_2 contents vary, respectively, between <0.09 wt %, and 0.02–0.14 wt % (mean. 0.11 wt %) in the dark areas and 0.11–0.45 wt % (mean. 0.25 wt %) and 0.04–0.28 wt % (mean. 0.20) in the bright areas. The SO_3 abundance changes from 0.004 to 0.17 wt % (mean. 0.07 wt %) in the dark areas, to 0.08 to 0.72 wt % (mean. 0.22 wt %) in the bright areas. The CaO and P_2O_5, which have covariance with Na, Si, and LREEs, range from 53.96–55.98 wt % (mean. 55.39) and 39.86–42.97 wt % (mean. 41.60 wt %) in the dark areas and from 52.72–55.12 wt % (mean. 53.92 wt %) and 39.61–42.24 wt % (mean. 41.22 wt %) in the bright areas, respectively.

In the MAA-marginal ore apatite, the Na_2O and SiO_2 contents vary between <0.10 wt % and 0.015–0.21 wt % (mean. 0.17 wt %), respectively, in the dark areas and 0.12–0.37 wt % (mean. 0.23 wt %) and 0.14–0.35 wt % (mean. 0.22 wt %) in the bright areas. The SO_3 contents vary from 0.02–0.09 wt % (mean. 0.05 wt %) in the dark areas to 0.09–0.35 wt % (mean. 0.20 wt %) in the bright areas. The abundances of CaO and P_2O_5 change respectively from 54.40 to 56.44 wt % (mean. 55.57 wt %) and 41.19 to 42.97 wt % (mean. 42.09 wt %), in the dark areas, and from 53.01 to 55.25 wt % (mean. 53.97 wt %) and 40.30 to 42.84 wt % (mean. 41.60 wt %) in the bright areas.

The apatite veins in the inner parts of the main ore body, or MAV-inner ore apatites, contain <0.07 wt % Na_2O and <0.29 wt % SiO_2 in the dark areas and 0.05–0.30 wt % (mean. 0.17 wt %) Na_2O and 0.004–0.32 wt % (mean. 0.16 wt %) SiO_2 in the bright areas. The SO_3 contents vary from <0.09 wt % in the dark areas and from 0.03 to 0.23 wt % (mean. 0.15 wt %) in the bright areas. The CaO and P_2O_5 contents range, respectively, between 55.14–56.37 wt % (mean. 55.68 wt %) and 41.60–42.64 wt % (mean. 42.18) in the dark areas and 54.35–56.21 wt % (mean. 55.06 wt %) and 41.36–42.53 wt % (mean. 41.70 wt %) in the bright areas.

Figure 10 shows the relationships in a binary $Na_2O + SiO_2 + Y_2O_3$ versus $CaO + P_2O_5$ diagram for the three apatite types. For each apatite type, the bright areas show higher Na_2O, SiO_2, and Y_2O_3 contents compared to the dark areas. Geochemical characteristics of Sr and Y can define apatite compositional fields for different rock type compositions [54]. The Sr and Y values in the apatites range between <372 ppm and <1310 ppm, respectively, and mostly plot in the granitoids and iron ore fields (Figure 11a). On the Mn vs. Sr diagram, the apatites plot in the granitoid, granite pegmatite, and iron ore fields (Figure 11b). Our EPMA data are consistent with those reported from apatites from other Kiruna-type iron deposits [13,35,36,53]. The concentrations of V, Mn, and Mg have been used to discriminate IOCG- and Kiruna-type deposits [55]. The Mn contents from the Chadormalu apatites are lower than those from typical IOCG-type deposits and are similar to Kiruna-type systems (Figure 12).

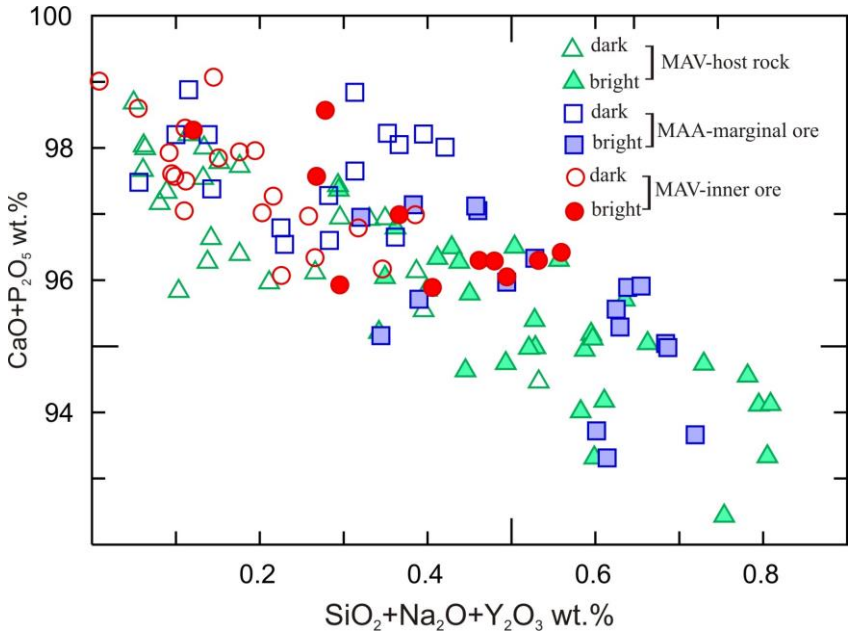

Figure 10. $SiO_2 + Na_2O + Y_2O_3$ versus $CaO + P_2O_5$ plot of Chadormalu apatites.

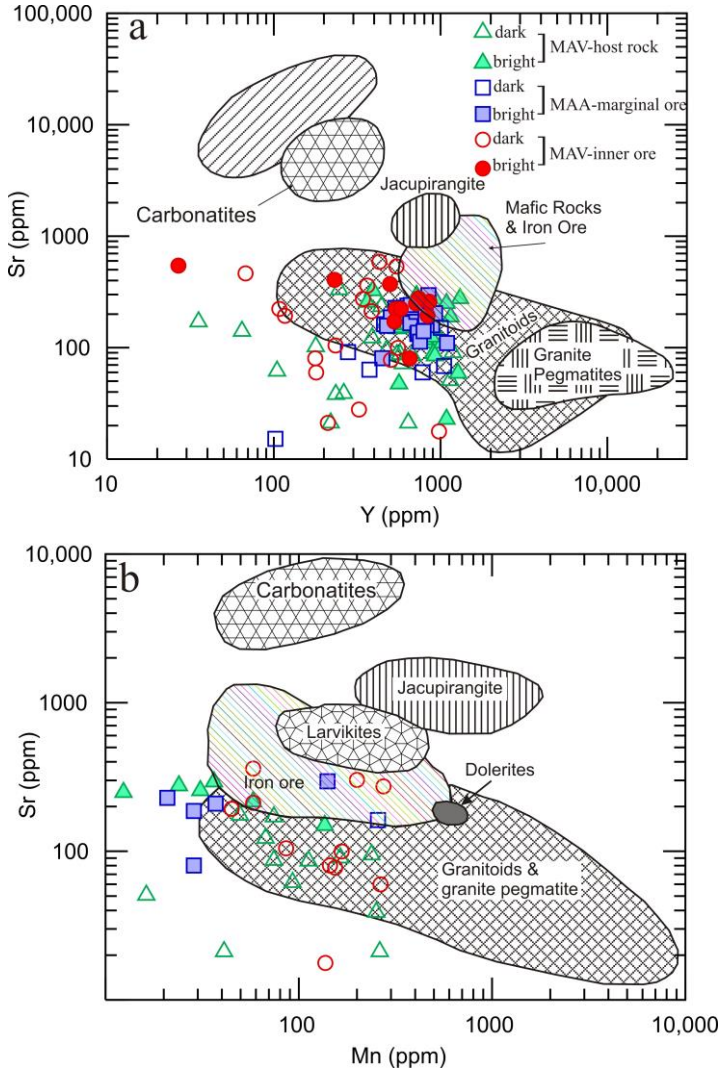

Figure 11. Sr versus Y (**a**) and Sr versus Mn (**b**) plots for Chadormalu apatites. Note that most data plot in the granitoid and iron ore fields. The fields were defined by [54].

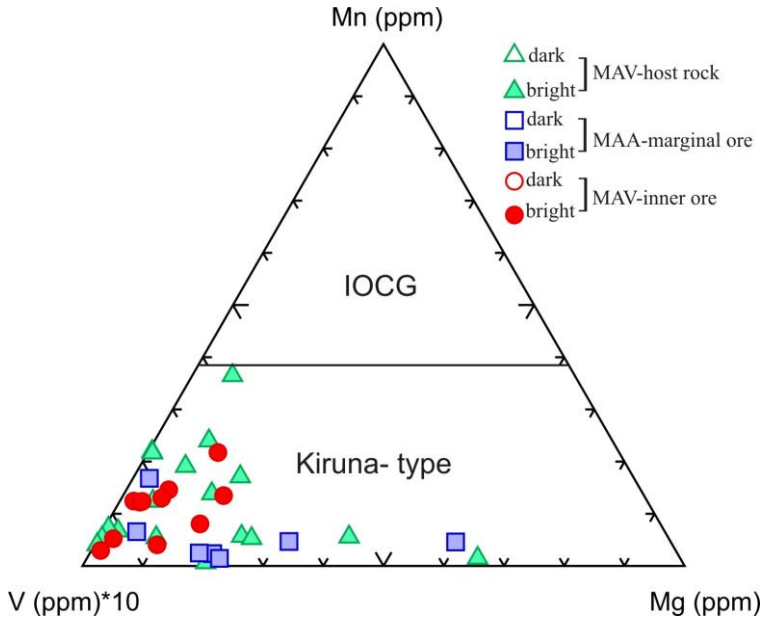

Figure 12. Mg-V-Mn ternary plot, showing boundary between apatites from IOCG and Kiruna-type IOA deposits [55]. Chadormalu apatites plot in the Kiruna-type field.

4.2.2. LA-ICP-MS

Trace-element compositional data on BSE bright and dark areas (114 points) was obtained for bright and dark spots in the three different apatite types to evaluate any spatial control on relative element abundances. The results are presented in Tables 5–7, and graphically shown in Figure 13. The MAV-host rock apatite type has ΣREE values ranging between 9077–39,212 ppm in the bright areas to 794–1874 ppm in the dark areas. For the MAA-marginal type apatites, the ΣREE ranges from 10,885–33,750 ppm in the bright areas to 2732–8508 ppm in the dark areas. The MAV-inner ore apatites contain ΣREE ranging from 10,529–27,198 ppm and 2633–8873 ppm in the bright and dark apatites, respectively. The La_N/Yb_N ratio in apatite from MAV-host rocks ranges between 13.5–27.5 and 5.7–17.68 in the bright and dark areas, respectively. This ratio varies in MAA-marginal ore apatite type from 21.17–58.51 in the bright areas to 4.10–18.24 in the dark areas. The MAV-inner ore apatites show La_N/Yb_N ratios from 19.3–51.4 in the bright areas to 6.2–19.4 in the dark areas. On the ΣREE vs. La_N/Yb_N plot, the SEM-bright areas show higher La_N/Yb_N ratios and higher REE contents, compared to the dark areas (Figure 13).

Chondrite-normalized patterns of REE in the dark and bright areas in various apatite types show negative Eu anomalies, which are more pronounced in the dark areas (Figure 14a–c). The Eu/Eu* (Eu/Eu* = $Eu_N/[(Sm_N)(Nd_N)]^{1/2}$) ratios for the dark and bright areas vary from 0.18–0.30 to 0.17–0.32 in the MAV-host rock apatite, from 0.25–0.30 to 0.28–0.32 in the MAA-marginal ore apatite, and from 0.14–0.27 to 0.26–0.29 in the MAV-inner ore apatite, respectively.

Table 5. LA-ICP-MS data (ppm) for bright and dark apatites from Chadormalu MAV-host rock apatite type.

Element	Bright (n = 35)		Dark (n = 23)	
	Mean	SD	Mean	SD
Y	1520.4	683.1	987.8	344.3
La	3009.2	1554.1	1214.4	571.2
Ce	7383.3	3626.7	3101.2	1414.1
Pr	794.2	367.0	346.5	156.0
Nd	2914.9	1270.6	1343.0	564.1
Sm	414.8	158.5	224.4	85.1
Eu	33.4	11.2	18.4	7.3
Gd	360.7	139.7	215.4	75.7
Tb	44.3	18.4	27.8	9.5
Dy	242.0	107.3	155.2	52.3
Ho	45.5	21.5	29.7	9.8
Er	114.6	58.9	74.9	23.4
Tm	13.4	7.8	8.8	2.3
Yb	77.9	49.1	52.1	11.1
Lu	9.7	6.5	6.7	1.6
Pb	4.0	0.8	2.6	2.1
Th	94.4	36.3	58.1	30.3
U	1.8	0.7	1.1	0.7
ΣREE	12,448.7	5744.4	5604.2	2386.0

SD = Standard deviation.

Table 6. LA-ICP-MS data (ppm) for bright and dark apatites from Chadormalu MAA-marginal ore apatite type.

Element	Bright (n = 14)		Dark (n = 7)	
	Mean	SD	Mean	SD
Y	1260.8	170.2	779.8	320.6
La	5109.4	4658.2	734.4	529.2
Ce	12,247.1	11,984.8	2110.6	1176.4
Pr	1267.4	1169.9	272.2	133.8
Nd	4278.8	3497.3	1154.4	477.2
Sm	548.8	326.9	213.4	76.0
Eu	47.7	20.2	18.7	6.8
Gd	428.6	164.2	204.8	73.7
Tb	47.3	10.3	25.3	9.4
Dy	228.2	27.2	131.7	51.4
Ho	41.0	5.1	24.4	9.9
Er	96.1	14.9	58.7	24.5
Tm	11.0	2.0	6.6	2.8
Yb	60.7	12.8	35.0	14.8
Lu	7.6	1.6	4.2	1.8
Pb	5.6	5.8	1.5	0.6
Th	186.2	251.7	26.8	19.2
U	2.8	2.5	0.5	0.3
ΣREE	24,419.7	21,810.4	4994.4	2449.8

SD = Standard deviation.

Table 7. LA-ICP-MS data (ppm) for bright and dark apatites from Chadormalu MAV-inner ore apatite type.

Element	Bright (n = 6)		Dark (n = 29)	
	Mean	SD	Mean	SD
Y	1305.2	354.0	701.5	196.1
La	3466.7	1367.3	713.1	336.8
Ce	8368.3	3152. 6	2104.8	804.0
Pr	906.3	330.7	254.6	89.3
Nd	3313.3	1162.3	1052.5	334.5
Sm	468.3	148.3	174.1	50.9
Eu	40.3	13.2	14.1	5.0
Gd	383.3	105.3	166.7	46.6
Tb	44.0	11.2	20.8	5.9
Dy	223.1	56.4	111.5	32.1
Ho	40.5	10.4	21.2	6.1
Er	97.7	26.2	52.3	15.1
Tm	11.2	3.3	6.0	1. 8
Yb	63.6	19.7	33.6	10.5
Lu	7.9	2.5	4.1	1.4
Pb	4.2	1.1	1.6	0.7
Th				
U	2.1	0.5	0.6	0.4
ΣREE	17,434.6	6346.7	4729.7	1682.4

SD = Standard deviation.

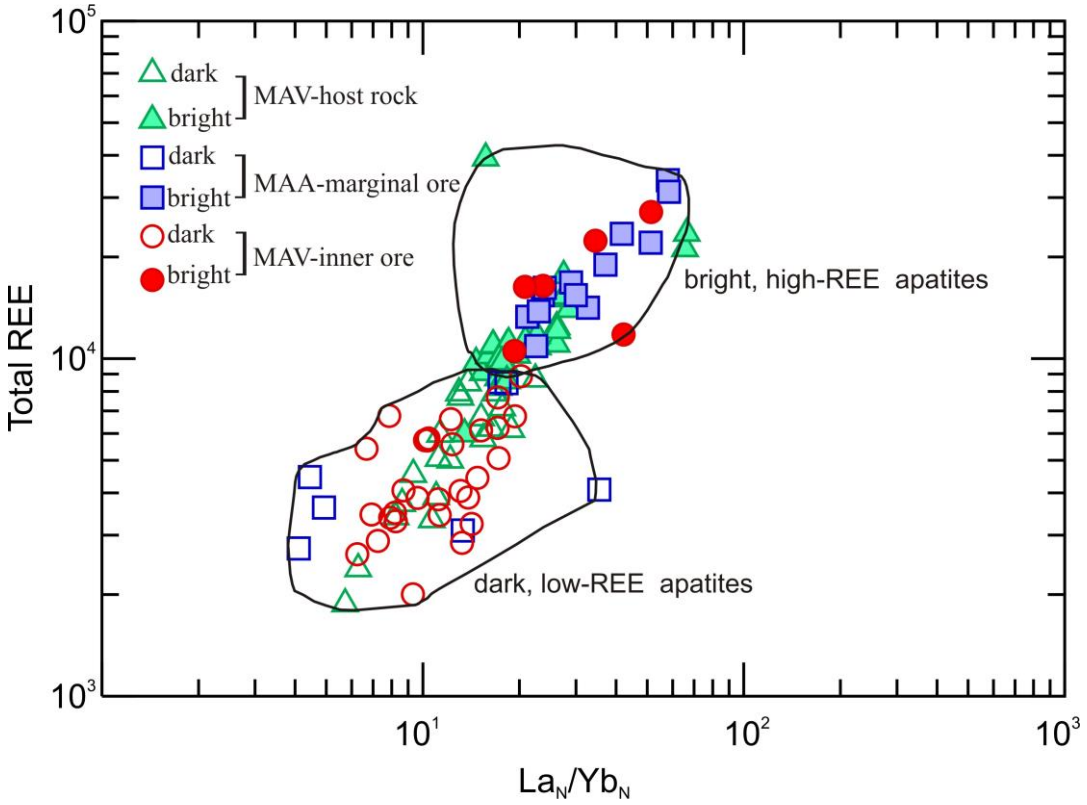

Figure 13. La_N/Yb_N ratio (as monitor of the fractionation degree of the REE) vs. total REE concentrations (ppm) for the Chadormalu apatites.

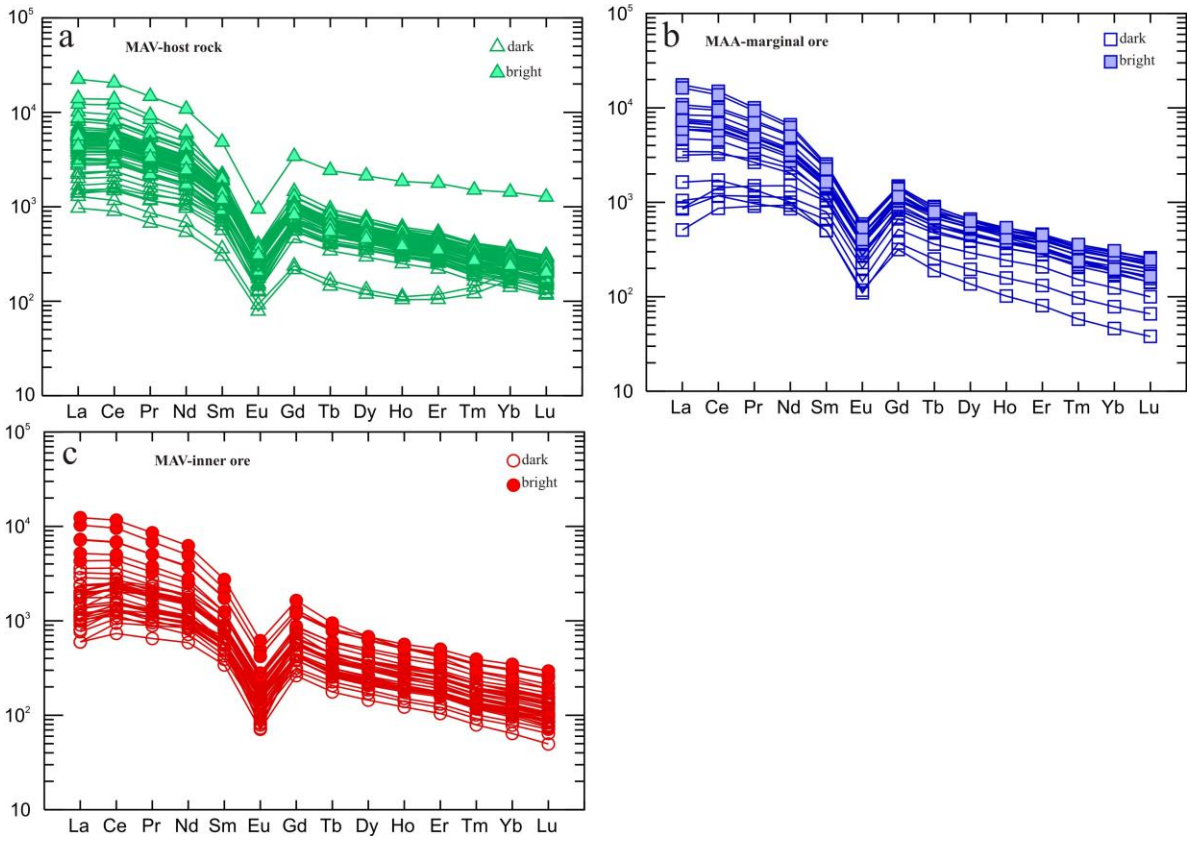

Figure 14. Chondrite-normalized REE patterns for dark and bright areas in the three different apatite types. (**a**) AMV-host rock; (**b**) MAA-marginal ore; (**c**) MAV-inner ore. Chondrite values after [56].

4.2.3. U-Pb Geochronology

In addition to the trace-element data described above, apatite crystals from 6 samples representing the main apatite types were analyzed for U-Th-Pb abundances and isotope ratios (122 spots) (Figure 15, Tables 8 and 9). Several spots (n = 25/147) for which ablation was catastrophic (e.g., intersected fracture), or that encountered obvious inclusions or displayed other obvious analytical artifacts were rejected. The analyses cover the dark and bright areas, which both have low U contents (0.1–5.6 ppm). The majority of the analyses contained U-rich spikes interpreted to represent micro-scale monazite inclusions; attempts were made to exclude these spikes during offline data reduction. A small subset of spots from SEM-BSE bright areas (n = 6/80) in apatite crystals define a lower intercept age of 490 ± 27 Ma and a common-Pb intercept of 0.862 ± 0.130. Other data from the same domains show a dispersion to younger ages with a minimum age of 246 ± 17 Ma (MSWD = 0.67) calculated for a subset (n = 11/80) of the youngest spots assuming the same common-Pb $^{207}Pb/^{206}Pb$ value as the older domains. The darker REE-depleted domains define a more coherent array with a lower intercept age of 437 ± 12 Ma (n = 46/77 spots) and a common-Pb intercept of 0.849 ± 0.030.

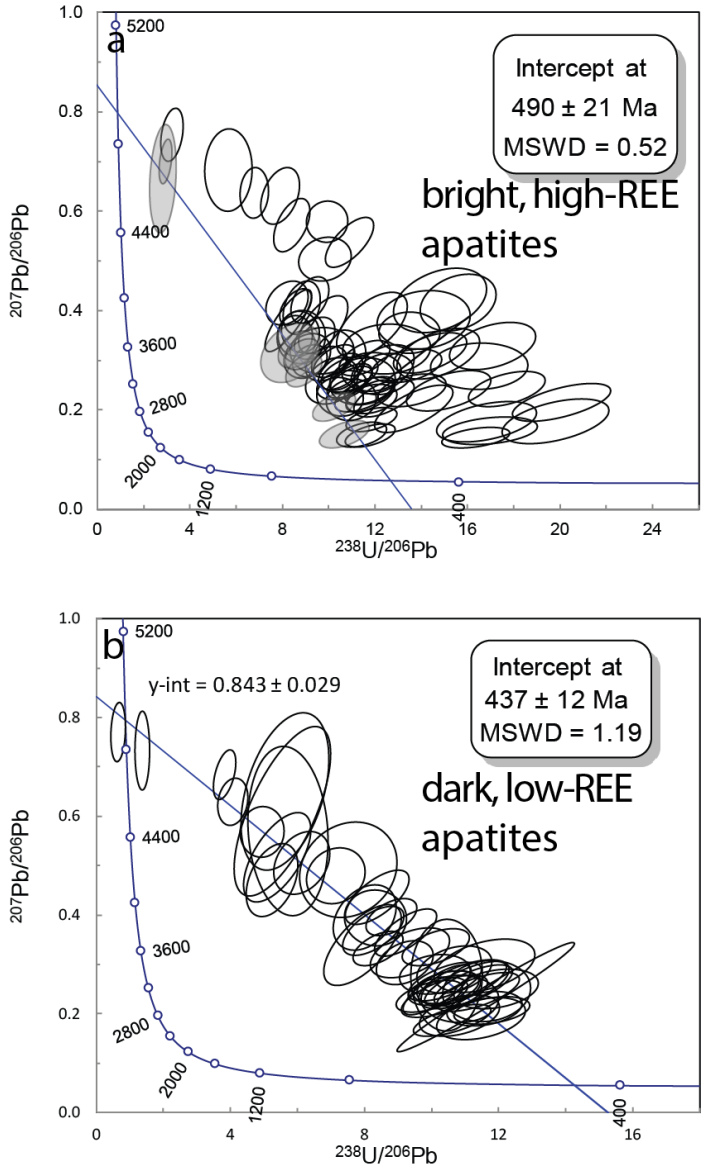

Figure 15. (**a**,**b**) Concordia diagrams for the bright, high-REE and the dark, low-REE apatites from Chadormalu (data from Tables 8 and 9).

Table 8. U-Pb-Th isotope compositions and isotope ratios for the bright, high-REE apatites, Chadormalu deposit (abundances in ppm).

Samples	^{234}Th	^{238}U	Th/U	^{238}U/^{206}Pb	2σ	^{207}Pb/^{206}Pb	2σ	err. cor	Samples	^{234}Th	^{238}U	Th/U	^{238}U/^{206}Pb	2σ	^{207}Pb/^{206}Pb	2σ	err. cor
Cha24-2	116	2.73	43	16.4	1.2	0.145	0.02	0.44	Cha2	93	1.2	77	10.4	1	0.3	0.05	0.21
Cha2	85	1.85	46	11.8	0.9	0.149	0.02	0.53	Cha2	126	1.44	88	11.6	0.9	0.304	0.03	0.53
Cha2-1	93	1.95	47	11.4	0.9	0.15	0.02	0.44	Cha2	98	1.86	53	9.07	0.8	0.309	0.04	0.24
Cha24-2	67	1.14	59	10.7	0.9	0.154	0.02	0.51	Cha2	164	1.4	117	14.8	1.5	0.313	0.04	0.47
Cha24-2	93	2.27	41	17	1.7	0.158	0.02	0.31	Cha24-2	106	1.81	59	14.4	1.3	0.315	0.03	0.53
Cha24-2	95	1.57	61	16.8	1.8	0.176	0.03	0.44	Cha2	106	1.28	83	8.84	0.6	0.315	0.03	0.42
Cha24-2	132	2.09	63	19.8	1.9	0.177	0.04	0.49	Ch15	75	1.38	54	8.33	1	0.317	0.05	0.32
Cha1-1	116	2.51	46	11.9	0.9	0.181	0.02	0.48	Cha24-2	131	1.78	74	9.71	1.1	0.319	0.04	0.05
Cha24-2	119	2.08	57	13.7	1.4	0.202	0.04	0.69	Cha24-2	88	2.04	43	12.5	1.6	0.322	0.04	0.07
Cha2	105	1.47	72	10.2	0.8	0.209	0.02	0.53	Cha2	107	1.03	104	14.3	1.5	0.323	0.05	1
Cha2	256	5.6	46	20.1	1.7	0.215	0.03	0.61	Ch15	96	1.7	57	8.58	0.7	0.324	0.03	0.37
Cha2-1	77	1.48	52	11	0.9	0.22	0.03	0.09	Cha24-2	145	2.89	50	17.1	1.5	0.328	0.04	0.41
Ch15	97	1.71	56	11.9	0.9	0.222	0.02	0.31	Ch15	134	1.63	82	9.4	0.7	0.344	0.04	0.41
Cha2	105	1.55	68	12.4	1.1	0.224	0.03	0.57	Cha2	76	1.01	75	8.82	0.9	0.347	0.04	0.04
Cha2	65	1.48	44	10.5	0.8	0.227	0.03	−0.08	Cha2	44	1.56	28	8.55	0.6	0.349	0.03	0.01
Cha1-1	111	2.07	54	11.8	0.9	0.228	0.03	0.6	Cha1-2	85	2.32	37	13.5	1.1	0.355	0.03	0.02
Cha1-1	100	1.69	59	11.6	1.1	0.231	0.03	0.6	Cha1-1	119	2.18	55	8.8	0.7	0.357	0.03	−0.07
Cha2	123	2.12	58	11.7	0.9	0.239	0.02	0.44	Cha1-1	123	1.07	115	11.9	1.2	0.371	0.05	0.57
Cha1-2	98	2.07	47	15.2	1.5	0.239	0.03	0.51	Cha2	90	1.16	78	9.77	0.9	0.372	0.05	0.6
Cha1-2	94	2.06	46	13.6	1.2	0.24	0.03	0.39	Cha24-2	78	1.27	62	8.26	0.8	0.38	0.05	0.81
Cha1-1	141	3.75	38	17.7	1.4	0.242	0.03	0.49	Cha1-2	116	1.73	67	14.1	1.7	0.382	0.05	0.14
Cha2	75	1.77	42	10.6	0.9	0.25	0.02	0.3	Cha2	80	1.52	53	8.84	0.7	0.405	0.04	0.31
Cha1-1	102	2.08	49	10.9	0.8	0.256	0.03	0.6	Cha2	134	1.95	69	8.58	0.6	0.407	0.03	0.5
Cha1-1	89	1.6	56	11.5	1.2	0.257	0.04	0.14	Cha24-2	113	2.16	52	15.6	1.3	0.416	0.05	0.28
Cha2	40	1.18	34	10.1	0.9	0.258	0.04	0.28	Cha1-2	128	1.51	85	8.2	0.7	0.416	0.04	0.29
Cha2	119	1.76	67	11	0.7	0.263	0.03	0.53	Cha2	152	1.62	94	14.8	1.7	0.42	0.05	0.35
Cha2	94	1.89	50	10.9	1	0.272	0.03	0.42	Cha2	134	1.57	85	9.19	0.7	0.421	0.04	0.44
Cha1-2	113	2.59	44	12.4	1	0.272	0.03	0.21	Cha24-2	122	2.83	43	9.84	0.9	0.503	0.04	0.14
Cha1-1	100	2	50	11.9	1.1	0.277	0.03	0.04	Cha24-2	130	2.48	52	10.9	0.9	0.537	0.04	0.67
Ch15	122	1.78	68	10.5	0.8	0.278	0.03	0.49	Cha24-2	101	1.93	52	8.42	0.6	0.572	0.04	0.52
Cha1-2	118	1.53	77	12.4	1.1	0.282	0.04	0.43	Cha1-2	150	6.45	23	9.93	0.7	0.579	0.03	0.03
Cha2	95	1.75	54	8.91	0.7	0.283	0.03	0.45	Cha24-2	103	1.88	55	7.91	0.7	0.631	0.05	0.37
Cha2	175	3.81	46	16.5	1.7	0.288	0.04	0.04	Cha24-2	93	2.18	42	6.78	0.5	0.637	0.04	0.07
Cha1-2	77	2.24	34	13.4	1.2	0.289	0.03	0.38	Cha24-2	66	0.45	145	2.82	0.5	0.668	0.09	0.21
Cha2	94	1.75	54	9.91	0.7	0.293	0.03	0.32	Cha24-2	184	1.29	143	5.68	0.8	0.683	0.07	0.03
Cha2	62	1.53	41	10.3	0.7	0.298	0.03	0.56	Cha1-2	77	1.49	51	2.92	0.2	0.702	0.04	0.41
Ch15	113	1.55	73	9.2	0.6	0.299	0.03	0.25	Cha24-2	100	0.91	109	3.23	0.4	0.754	0.04	0.33

Table 9. U-Pb-Th isotope compositions and isotope ratios for the dark, low-REE apatites, Chadormalu deposit (abundances in ppm).

Samples	^{234}Th	^{238}U	Th/U	^{238}U/^{206}Pb	2σ	^{207}Pb/^{206}Pb	2σ	err. cor	Samples	^{234}Th	^{238}U	Th/U	^{238}U/^{206}Pb	2σ	^{207}Pb/^{206}Pb	2σ	err. cor
Cha1-1	25	0.49	51	5.71	1	0.57	0.14	−0.12	Cha2	58	1.25	47	11.6	1.1	0.246	0.05	0.1
Cha1-1	59	1.4	42	11.6	1.2	0.298	0.04	0.41	Cha2	64	1.27	50	9.23	0.8	0.364	0.04	0.7
Cha1-1	37	1.29	29	3.83	0.3	0.684	0.04	0.49	Cha2	47	1.13	41	7.14	0.7	0.479	0.05	0.14
Cha1-1	43	1.59	27	4.07	0.4	0.629	0.04	0.18	Cha2	66	1.08	61	11.4	1	0.245	0.03	0.65
Cha1-1	27	0.74	37	7.94	0.9	0.339	0.07	0.66	Cha2	44	0.98	44	10.4	0.9	0.265	0.03	0.62
Cha1-1	64	1.56	41	4.95	0.5	0.569	0.04	0.03	Cha2	54	1.06	51	11	1.1	0.26	0.04	0.6
Cha1-1	60	1.2	50	6.13	0.7	0.505	0.05	0.29	Ch15	44	0.77	58	10.9	1	0.196	0.03	0.4
Cha1-1	49	0.95	52	5.24	0.6	0.471	0.06	0.4	Ch15	39	0.65	60	11.5	1.1	0.19	0.04	0.37
Cha2	26	0.46	57	5.41	0.8	0.517	0.07	0.62	Ch15	88	1.38	64	11.6	0.9	0.21	0.03	0.29
Cha2	21	1.23	17	11.3	1	0.257	0.03	0.68	Ch15	56	1.04	54	10.9	0.9	0.231	0.04	0.01
Cha24-2	21	0.2	107	0.65	0.2	0.77	0.05	0.16	Ch15	103	1.5	69	10.1	0.8	0.335	0.03	0.52
Cha1-2	28	0.38	75	1.37	0.2	0.733	0.07	0	Ch15	109	1.47	74	11.9	1	0.25	0.03	0.29
Cha1-2	21	0.71	30	8	0.8	0.395	0.05	0.33	Ch15	82	1.42	58	11.8	0.9	0.207	0.02	0.37
Cha1-2	25	0.81	31	10.4	1.1	0.235	0.04	0.65	Ch15	78	1.06	74	9.35	1	0.323	0.04	0.48
Cha1-2	48	0.74	65	7.52	1.2	0.491	0.08	0.15	Ch15	75	1.19	63	8.33	0.8	0.394	0.05	−0.03
Cha1-2	35	1.31	26	11.6	2.2	0.234	0.09	0.98	Ch15	63	0.98	64	11	1	0.261	0.04	0.74
Cha1-2	21	0.41	50	5.56	1.2	0.61	0.14	0.68	Ch15	85	0.97	88	10.2	0.8	0.249	0.04	0.77
Cha1-2	59	0.89	67	8.26	0.8	0.368	0.04	0.6	Ch15	84	1.1	76	10.7	0.9	0.29	0.04	0.32
Cha2	46	1.21	38	10.6	1	0.187	0.03	0.65	Ch15	66	0.98	68	10.4	0.9	0.278	0.09	0.02
Cha2	25	0.98	26	8.38	0.8	0.436	0.05	0.67	Ch15	86	1.45	59	10.5	0.8	0.253	0.03	0.31
Cha2	23	1.71	14	10.2	0.7	0.246	0.02	0.35	Ch15	105	1.38	76	9.21	0.7	0.303	0.04	0.33
Cha2	65	1.65	39	8.8	0.6	0.396	0.03	0.5	Ch15	89	1.75	51	10.1	0.9	0.28	0.03	0.19
Cha2	58	1.36	42	8.4	0.6	0.332	0.03	0.54	Ch15	90	1.44	63	9.93	0.8	0.235	0.03	0.53
Cha2	24	0.36	65	5.62	1.1	0.65	0.13	0.41	Ch15	89	1.27	70	10.4	0.8	0.253	0.03	0.36

5. Discussion

5.1. Textural and Mineral Chemical Evidence

Textures and chemical compositions of apatite may change due to metasomatic events over a wide range of temperatures and pressures from the mantle to surficial environments, thus making apatite an important fingerprint of metasomatic processes [13]. The three main apatite types in the Chadormalu IOA deposit show similar textural features including the occurrence of bright and dark SEM-BSE apatite spots containing monazite and xenotime inclusions. Formation of larger monazite grains at the expense of smaller grains; intergrowth of monazite with magnetite, and development of allanite are due to late stage fluid-aided reaction of monazite with surrounding silicate minerals (cf. [1,13,53,54,57,58]). These features appear to be common in other Bafq district magnetite-apatite deposits, such as Esfordi, Se-Chahun, Choghart, and Mishdovan [18,20,28,35,36,52].

The EPMA and LA-ICPMS data indicate that the SEM-BSE dark spots or areas in each three types of apatites are strongly depleted in certain other elements, including Si, Na, Cl, and F and in REE. The depleted dark areas developed upon alteration and significant REE leaching from the original apatite. The alteration and associated REE leaching was not a pervasive reaction, leaving behind a mixture of original REE-rich (bright areas) and REE-poor (dark areas) zones in the apatite crystal. The alteration and element remobilization occurred via interaction of percolating fluids with the earlier generations of apatite [53]. However, leached REE were incorporated into other mineral inclusions, LREE preferentially incorporate into monazite and HREE into xenotime (Figure 13)

Similar REE-depleted, dark domains within apatite, accompanied by monazite inclusions, are reported by Harlov et al. (2002) [53] from the Kirunavaara deposit, northern Sweden. The occurrence of fine monazite and/or xenotime inclusions in apatite and its grain boundaries have also been reported from metamorphosed rocks (e.g., [14,59,60]). The occurrence of monazite and xenotime in REE-depleted apatites has been observed in some other Bafq district magnetite-apatite deposits [18,20,28,35,36,52].

According to experimental studies of Harlov 2015 [13], metasomatic alteration leads to the preferential removal of Na and/or Si and LREE from primary apatites. Sodium and Si deficiency in the apatite is cross-correlated with the nucleation and growth of monazite and/or xenotime inclusions. It will occur due to two general mass transfer reactions, including $Si^{4+} + (Y + REE)^{3+} = P^{5+} + Ca^{2+}$ or $Na^{+} + (Y + REE)^{3+} = 2Ca^{2+}$ [14]. The REE contents of the monazite grains will reflect the REE concentrations of the primary apatites (e.g., [61]). The reaction, which proceeds in an open system, would lead to relative enrichment of Ca and P in apatite zones that are depleted in LREE (dark areas). According to Putnis (2009) [62] the formation and growth of monazite and xenotime inclusions or grains along rims or cracks in apatite results from coupled dissolution-reprecipitation processes due to metasomatic alteration of apatites over a wide P-T range starting at near-surface pressures and 100 °C.

However, monazite nucleation is strongly dependent on the reactivity properties of fluid and the apatite, and also the amount of REEs available [63,64]. Dissolution-reprecipitation occurs in the interconnected micro- to nano-scale fractures and porosity in the host apatites. They allow fluids to infiltrate [62,65] and rapid (hours-days) nucleation of monazite and/or xenotime inclusions [13]. Recrystallization of altered regions can impede or cease the fluid aided coupled dissolution-reprecipitation. This is supported by our data for Chadormalu apatites (see Figures 10 and 13). Dissolving portions of apatite creates space for the nucleation and growth of monazite inclusions (cf. [53]). Fewer and larger monazite inclusions in brecciated apatites (MAA-marginal ore) show that REE leaching is largely a temperature- and deformation-related process. Large allanite crystals formed in the first type of apatites could be related to incorporation of liberated LREE.

5.2. Comparison with Magnetite Alteration

Alteration and remobilization features comparable to those in apatite has recently been documented through SEM and EPMA studies on different magnetite types from the Chadormalu deposit [22]. Primary magnetite (Mag 1) formed initially from magmatic hydrothermal fluids was enriched in Si, Al, and Ca, whereas secondary magnetite (Mag 2) with higher Fe and lower Si, Al, and Ca contents were generated through interaction of the primary ore with infiltrating fluids of non-magmatic origin.

5.3. Nature of Fluids

Many studies on the IOCG and IOA deposits have provided evidence of fluid mixing during the ore-forming processes ([6], and references therein). Various studies of IOA deposits have proposed different petrogenetic models including magmatic (e.g., [58,66]), magmatic-hydrothermal [67], hydrothermal (-metasomatic) (e.g., [68–70]), and sedimentary exhalative (e.g., [71,72]). For the Bafq district, some researchers have referred to a magmatic model [17,28,73,74], whereas Torab and Lehmann (2007) [35], Jami (2005) [21], and Daliran (2010) [19] considered high-T hydrothermal fluids as being responsible for generation of some Bafq IOA deposits. Taghipour et al. (2013) [75] argued that mixing of magmatic and non-magmatic fluids caused iron oxide mineralization and hydrothermal alteration in the Choghart deposit. However, Mohseni and Aftabi (2015) [76] have presented evidence that the Central Iran iron deposits were formed as glaciogenic banded iron formation (Rapitan BIF).

Fluid inclusion studies on Chadormalu apatites [31] from vein and massive ores show a range of homogenization temperatures from 266° to 580 °C and 208° to 406 °C, and salinities from 0.5 to 10.7 wt % NaCl equiv., and 0.3 to 24.4 wt % NaCl equiv., respectively. From fluid inclusion data, it can be inferred that progressive evolution of a single source fluid and/or mixing of two different fluids, one with lower salinity and higher temperature and another with higher salinity and lower temperature were involved in the generation of massive- and vein-type type ores, respectively [31].

As discussed by Harlov et al. (2002) [53], magnetite-apatite ore deposits may have experienced some subsequent stages of fluid–rock interactions. The F^-, Cl^-, OH^-, and SO_3 contents in apatite, coupled with the possible presence of monazite and xenotime inclusions, can serve as valuable "fingerprints" for recording alteration events in rocks. Fluids with a large range of compositions can affect the apatite through REE leaching and development of monazite inclusions. Various acids, such as HCl or H_2SO_4 [13], KCl brines, pure H_2O, and $H_2O + CO_2$ have been shown to facilitate monazite or xenotime inclusion formation, whereas NaCl and $CaCl_2$ brines inhibit inclusion formation.

The concentration of LREE in the NaCl brines increases with X_{NaCl}, pressure, and temperature, because complexing of REE with Cl^- stops complexing with PO_4^{3-} and F^- (e.g., [63,77,78]). Also, Na and Ca can enter the apatite structure and maintain the charge balance that prevents REE complexation. Harlov et al. (2002) [53] noted that inclusion-absent apatites, which are documented in Chilean IOA deposits, could have formed in the presence of Na-rich fluids preventing monazite formation. Monazite and/or xenotime inclusion formation is relatively P-T insensitive and can occur at conditions from 100 °C and <100 MPa. For different IOA deposits, there are extensive sodic and calcic alteration haloes around the magnetite-apatite mineralized zones, which formed from Na- and Ca-bearing fluids [4,7,79].

The extensive sodic and calcic alterations in the Chadormalu host rocks appear to be cogenetic with the formation of the primary apatite and associated magnetite that formed from Na- and Ca-enriched fluids at 490 ± 21 Ma. The secondary dark apatites with monazite inclusions formed through interaction of the primary apatite with KCl-H_2O fluids responsible for potassic alteration of the host rocks at 437 ± 12 Ma. The apatite-magnetite ore in Chadormalu experienced further interaction with fluids at 246 ± 17 Ma.

The common occurrence of monazite inclusions in apatites from the Bafq district IOA deposits, and the close spatial association with potassic alteration, suggest the involvement of KCl-rich fluids. Harlov et al. (2002) [53] proposed the introduction of residual HCl and/or $H_2SO_4^-$ enriched fluids along fluorapatite grain boundaries shortly after apatite crystallization in the Kiirunavaara IOA

deposit. Torab and Lehmann (2007) [35] suggested that alteration of apatite and monazite inclusions occurred due to a switch to a KCl^- dominant brine composition, consistent with potassic alteration. Jami et al. (2007) [20] considered that different fluids, ranging from a hot Na-K-Ca brine to progressively cooler and more dilute brines, contributed to the formation of Esfordi IOA deposit. Taghipour et al. (2015) [52] suggested a KCl-CO_2 dominated fluid for the Esfordi and Chadormalu IOA deposits and a NaCl-rich fluid for the inclusion-free apatites in the Choghart deposit.

According to various lines of evidence obtained from apatite andmagnetite, we propose three subsequent stages of fluid evolution, associated with mineralization and alteration in Chadormalu (Figure 16). Higher temperature, low salinity magmatic fluids were responsible for the primary magnetite-apatite mineralization (Mag 1 and bright apatites) with higher Si, Na, and REE contents (Figure 16a). These fluids were also responsible for the large-scale sodic-calcic alterations of the host rocks. During the next stage, the chemistry of the fluids would have become KCl enriched. This fluid was responsible for the formation of the secondary magnetites (Mag 2) due to a dissolution-reprecipitation process, along with REE + Y, Na, and Si leaching from the primary, bright apatite. This led to the formation of dark, low REE apatite and subsequent precipitation of monazite inclusions [80] (Figure 16b). Potassic alteration of the host rocks occurred during this stage. Continued fluid introduction in later stages was associated with the growth of the fine monazite inclusions and development of large monazite grains (Figure 16c). This is consistent with the younger ages (246 ± 17 Ma) obtained from some bright apatites. The activities of Na and Ca at these later stages must have been low; otherwise the formation of REE mineral inclusions would have been retarded [15,53]. Local potassic alteration, represented by K-feldspar, sericite, and biotite in the host rocks, as well as saturation of allanite in apatites, are related to these later stages.

The negative Eu anomalies in the Chadormalu apatites are consistent with the contribution of an oxidizing hydrothermal fluid, at least partly composed of seawater or continental non-magmatic saline fluids. Hydrothermal fluids without positive Eu anomalies have been interpreted to consist mostly of seawater and/or contaminated with sedimentary detritus [81,82]. The low Y contents in dark areas of the apatites formed due to fluid-aided alteration.

5.4. Timing of Apatite Alteration and Its Implication

Alteration of apatite, as documented for Chadormalu, appears to be a common feature in IOA type ore deposits (e.g., Kiirunavaara magnetite-apatite ore [53], Los Colorados iron oxide-apatite [83], and Se-Chahun magnetite-apatite deposit [36]). Such reequilibration and modification in Chadormalu ore was already documented for magnetite by Heidarian et al. [21]. The relative timing of apatite alteration in the IOA type deposits in the Bafq district and elsewhere, however, is controversial. While some studies show that the alteration occurred shortly after the primary apatite formation [35,36,42,53], monazite-bearing apatite grains have yielded U-Pb ages indicative of the occurrence of the alteration long after (on the scale of geological periods) the formation of the primary apatite [34,84]. Stosch et al. (2011) [34] reported U-Pb ages of 539–527 Ma for monazite-free apatites from Lakkeh Siah, Esfordi, Mishdovan, and Zarigan IOA type deposits in the Bafq district. The authors reported U-Pb ages ranging between 440 and 130 Ma for monazite inclusions in apatite. The latter age is similar to the 150–160 Ma ($^{39}Ar/^{40}Ar$) measured for potassic alteration in the host rocks [39]. However, using U-Pb data, Bonyadi et al. (2011) [36] determined an age of 510 ± 8 Ma for the Se-Chahun IOA deposit in the Bafq district. The Th-U-Pb data of monazite from Choghart deposit resulted in 515 ± 21 to 529 ± 21Ma [35]. Therefore, they [35] discussed that monazite inclusions formed during the later metasomatic events after Fe-P mineralization.

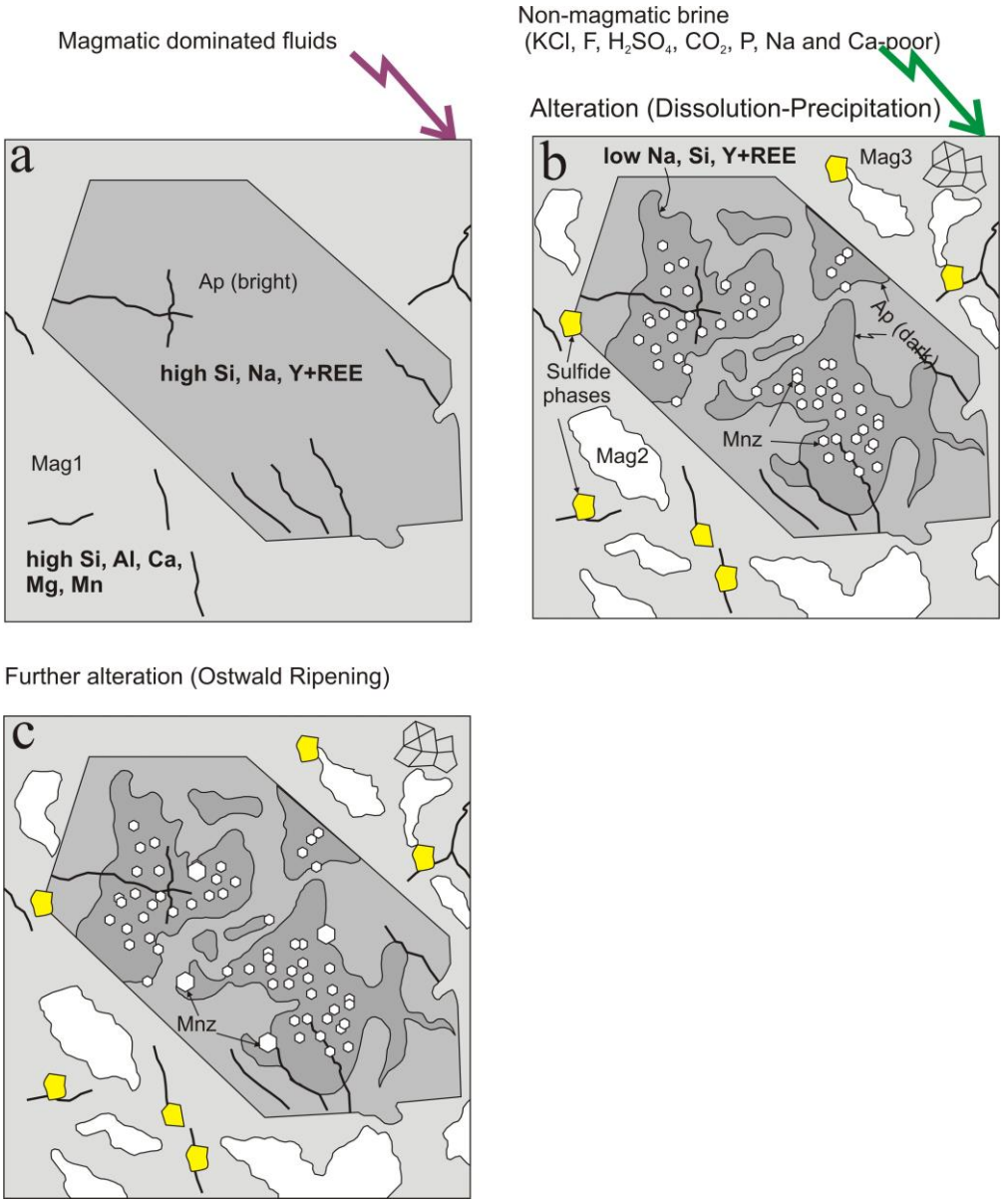

Figure 16. Schematic illustration for the mineralization and alteration history in the Chadormalu deposit. (**a**) Mineralization of the primary high Si magnetite (Mag 1) and REE-rich apatites (Ap, bright areas) from a magmatic dominated fluid at 490 ± 21 Ma; (**b**) Contribution of non-magmatic fluids enriched in KCl, F, H_2SO_4, CO_2, and P, which are Na- and Ca-deficient, in alteration process and related dissolution-reprecipitation stage, in the formation of secondary magnetite (Mag2). These fluids also interacted with the primary bright apatites, leading to remobilization and developing of Si-, Na-, and Y + REE-depleted dark areas in the apatites, as well as formation of monazite and rarely allanite crystals due to dissolution-reprecipitation process. This reaction stage probably occurred at 437 ± 12 Ma; (**c**) Further alteration caused growth of fine monazite inclusions.

The maximum age of 490 ± 21 Ma calculated for BSE- bright apatite in this study overlaps, within error, the lower end of previous age estimates for primary apatite in the Bafq district. On the other hand, the maximum age of 437 ± 12 Ma obtained from BSE-dark apatite provides an important evidence of a later process that led to development of dark domains and monazite inclusions; this appears to have occurred synchronous with the overprint potassic alteration in Chadormalu altered host rocks. This event was consistent with a regional extension and associated basin development and magmatism in Silurian, the evidence for which is provided by syenite intrusions and alkali basalts in Central Iran [85].

However, some spots from bright apatite type exhibit evidence for resetting of the U-Pb system defining an array with a lower intercept of 246 ± 17 Ma. Younger ages are generally assumed to reflect resetting of the U-Pb system due to later thermal or alteration events [86]. This might have occurred due to redistribution of radiogenic Pb from some parts of the apatite domains analyzed. These inconsistent ages reflect some resetting processes that caused Pb loss, which might be related to fluid flow associated with Triassic granite-tonalite magmatism, including the Saghand granitoid intrusions [25]. Several diabasic dykes in Chadormalu deposit, which are post mineralization, could have resulted in the younger ages of apatites.

6. Conclusions

Several lines of evidence including field observations, textural and chemical data from apatites from the Chadormalu IOA deposit in this study demonstrate that:

The Chadormalu IOA deposit is hosted within late Precambrian-Cambrian intrusive and extrusive rocks, which have undergone widespread sodic (albitization), calcic and ferroan (actinolitization), and potassic (K-feldspar and sericitization) alteration, as well as carbonatization. Apatite occurs as irregular veins within the internal parts of the main iron ore body, disseminated assemblages in the marginal part of the main ore body, and apatite veins in the altered host rocks. The SEM-BSE images of the apatites are indicative of primary bright areas and secondary dark areas with monazite/xenotime inclusions. The EPMA and LA-ICP-MS data reflect that the primary REE-rich fluorapatite was altered through a coupled dissolution and reprecipitation process during subsequent hydrothermal activity and (or) paleoweathering. NaCl-rich fluids containing F, SO_3, and P were responsible to large-scale sodic alteration in the host rocks and development of the primary fluorapatites enriched in REE + Y, Na, and Si. A KCl-enriched brine was most likely responsible for the dissolution and leaching of Na, Si, and REE + Y leaching from primary apatites (bright areas) and development of REE-depleted apatites (dark zones) containing monazite/xenotime inclusions. These KCl-bearing fluids caused local potassic alteration in upflow zones.

The U-Pb dating of different apatite types in the Chadormalu deposit yielded a minimum age of at least 490 ± 21 Ma for the primary apatite, which is similar to the ages reported from other Bafq iron deposits and also the Zarigan-type granite intrusions. From different lines of evidence, it can be concluded that the magmatic hydrothermal fluids associated with Zarigan-type intrusions were responsible for mineralization and for the large-scale sodic alteration. During later stages, KCl-enriched fluids were responsible for potassic hydrothermal alteration and lower T dissolution-reprecipitation that affected the primary magnetite and apatite assemblages and produced dark apatite patches. The U-Pb ages of these apatites yield 437 ± 12 Ma. These younger ages correspond to a regional extensional episode in the Posht-e-Badam block and elsewhere in Central Iran. This is supported by Silurian alkali basalts and syenitic intrusions. Extensional basins and related brines caused hydrothermal K-rich fluid flow and related dissolution-reprecipitation processes within the IOA ores. The younger Triassic ages (246 ± 17 Ma) also correspond to a prevailing extensional regime and associated high heat flow, fluid circulation, and recurring reequilibration of the original magnetite-apatite ore in Chadormalu.

Acknowledgments: Doug Hall (MMF at UNB) helped with the EPMA analysis of apatite. Brandon Boucher (UNB) helped with the LA ICP-MS analysis of apatite. David R. Lentz and Christopher R.M. McFarlane are supported by NSERC Discovery grants. We are particularly grateful for the constructive comments of anonymous reviewers.

Author Contributions: Hassan Heidarian did sampling and obtained field data under supervision of Saeed Alirezaei. David R. Lentz provided funds for analytical works and supervised the whole project. Christopher R. M. McFarlane carried out LA ICP-MS and U-Pb dating analyses. Sima Peighambari contributed writing and checking some parts of the manuscript. All authors contributed to presentation of data and writing of the manuscript.

Conflicts of Interest: The authors declare no conflict of interest.

References

1. Frietsch, R.; Perdahl, J.-A. Rare earth elements in apatite and magnetite in Kiruna-type iron ores and some other iron ore types. *Ore Geol. Rev.* **1995**, *9*, 489–510.
2. Williams, P. Classifying IOCG deposits. In *Exploring for Iron-Oxide Copper-Gold Deposits*: *Canada and Global Analogues*, 2nd ed.; Corriveau, L., Mumin, H., Eds.; Geological association of Canada, Short courses notes: Calgary, AB, Canada, 2010; Volume 20, pp. 11–19.
3. Meyer, C. Ore deposits as guides to geologic history of the earth. *Annu. Rev. Earth Planet. Sci.* **1988**, *16*, 147–171.
4. Hitzman, M.W.; Oreskes, N.; Einaudi, M.T. Geological characteristics and tectonic setting of Proterozoic iron oxide (Cu-U-Au-REE) deposits. *Precambrian Res.* **1992**, *58*, 241–287.
5. Groves, D.I.; Bierlein, F.P.; Meinert, L.D.; Hitzman, M.W. Iron oxide copper-gold (IOCG) deposits through earth history: Implications for origin, lithospheric setting, and distinction from other epigenetic iron oxide deposits. *Econ. Geol.* **2010**, *105*, 641–654.
6. Barton, M.D. Iron oxide (Cu-Au-REE-P-Ag-U-Co) systems. In *Treatise on Geochemistry*, 2nd ed.; Holland, H.D., Turekian, K.K., Eds.; Elsevier: Oxford, UK, 2014; Volume 13, pp. 513–536.
7. Williams, P.J.; Barton, M.D.; Johnson, D.A.; Fontboté, L.; De Haller, A.; Mark, G.; Oliver, N.H.; Marschik, R. Iron oxide copper-gold deposits: Geology, space-time distribution, and possible modes of origin. *Econ. Geol.* **2005**, *100*, 371–405.
8. Jonsson, E.; Harlov, D.E.; Majka, J.; Högdahl, K.; Persson-Nilsson, K. Fluorapatite-monazite-allanite relations in the Grängesberg apatite-iron oxide ore district, Bergslagen, Sweden. *Am. Mineral.* **2016**, *101*, 1769–1782.
9. Boyce, J.W.; Hervig, R.L. Apatite as a Monitor of Late-Stage Magmatic Processes at Volcán Irazú, Costa Rica. *Contrib. Mineral. Petrol.* **2009**, *157*, 135–145.
10. McCubbin, F.M.; Kaaden, K.E.V.; Tartèse, R.; Boyce, J.W.; Mikhail, S.; Whitson, E.S.; Bell, A.S.; Anand, M.; Franchi, I.A.; Wang, J. Experimental investigation of F, Cl, and OH partitioning between apatite and Fe-rich basaltic melt at 1.0–1.2 GPa and 950–1000 °C. *Am. Mineral.* **2015**, *100*, 1790–1802.
11. Krneta, S.; Ciobanu, L.C.; Cook, N.J.; Ehrig, K.; Kontonikas-Charos, A. Rare earth element behaviour in apatite from the Olympic Dam Cu-U-Au-Ag deposit, south Australia. *Minerals* **2017**, *7*, 135.
12. Pan, Y.; Fleet, M.E. Compositions of the apatite-group minerals: Substitution mechanisms and controlling factors. *Rev. Mineral. Geochem.* **2002**, *48*, 13–49.
13. Harlov, D.E. Apatite: A fingerprint for metasomatic processes. *Elements* **2015**, *11*, 171–176.
14. Pan, Y.; Fleet, M.E.; Macrae, N.D. Oriented monazite inclusions in apatite porphyroblasts from the Hemlo gold deposit, Ontario, Canada. *Mineral. Mag.* **1993**, *57*, 697–708.
15. Harlov, D.E.; Förster, H.-J. Fluid-induced nucleation of (Y + REE)-phosphate minerals within apatite: Nature and experiment. Part II. Fluorapatite. *Am. Mineral.* **2003**, *88*, 1209–1229.
16. Harlov, D.E.; Förster, H.-J.; Nijland, T.G. Fluid-induced nucleation of (Y + REE)-phosphate minerals within apatite: Nature and experiment. Part I. Chlorapatite. *Am. Mineral.* **2002**, *87*, 245–261.
17. Samani, B.A. Metallogeny of the Precambrian in Iran. *Precambrian Res.* **1988**, *39*, 85–106.
18. Daliran, F. Kiruna-Type Iron Oxide-Apatite Ores and Apatitites of the Bafq District, Iran, with an Emphasis on the REE Geochemistry of their Apatites. In *Hydrothermal Iron Oxide Copper-Gold and Related Deposits*; PGC Publishing: Adelaide, Australia, 2002; Volume 2, pp. 303–320.
19. Daliran, F. Lower Cambrian iron oxide-apatite-REE (U) deposits of the Bafq district, east-central Iran. In *Exploring for Iron-Oxide Copper-Gold Deposits*: *Canada and Global Analogues* 2nd ed.; Corriveau, L., Mumin, H., Eds.; Geological Association of Canada, Short Courses Notes: Calgary, AB, Canada, 2010; pp. 143–155.
20. Jami, M.; Dunlop, A.C.; Cohen, D.R. Fluid inclusion and stable isotope study of the Esfordi apatite-magnetite deposit, central Iran. *Econ. Geol.* **2007**, *102*, 1111–1128.
21. Jami, M. *Geology, Geochemistry and Evolution of the Esfordi Phosphate*: *Iron Deposit, Bafq Area, Central Iran*; University of New South Wales: Sydney, Australia, 2005.
22. Heidarian, H.; Lentz, D.; Alirezaei, S.; Peighambari, S.; Hall, D. Using the chemical analysis of magnetite to constrain various stages in the formation and genesis of the Kiruna-type Chadormalu magnetite-apatite deposit, Bafq district, central Iran. *Mineral. Petrol.* **2016**, *110*, 927–942.
23. Stöcklin, J. Stratigraphic Lexicon of Iran. Part I: Central, North and East Iran; Geological Survey of Iran: Tehran, Iran, 1971.

24. Haghipour, A.; Valeh, N.; Pelissier, G.; Davoudzadeh, M. *Explanatory Text of the Ardekan Quadrangle Map, 1:250,000*; Geological Survey of Iran: Tehran, Iran, 1977; Volume 8, p. 114.
25. Ramezani, J.; Tucker, R.D. The Saghand region, central Iran: U-Pb geochronology, petrogenesis and implications for Gondwana tectonics. *Am. J. Sci.* **2003**, *303*, 622–665.
26. Borumandi, H. P*etrographische und Lagerstättenkundliche Untersuchungen der Esfordi-Formation Zwischen Mishdovan und Kushk bei Bafq/Zentral Iran*; Rheinisch-Westfälische Technische Hochschule Aachen: Aachen, Germany, 1973.
27. Haghipour, A. *Geological Map of the Biabanak-Bafq Area* (*Scale 1:500,000*); Geological Survey of Iran: Tehran, Iran, 1977.
28. Foerster, H.; Jafarzadeh, A. The Bafq mining district in central Iran; a highly mineralized Infracambrian volcanic field. *Econ. Geol*. **1994**, *89*, 1697–1721.
29. Hahn, G.; Pflug, H. Ein neuer medusen-fund aus dem jung-Prakambrium von zentral-Iran. *Senckenb. Lethaea* **1980**, *60*, 449–461.
30. Samani, B. Saghand Formation, a riftogenic unit of upper Precambrian in central Iran. *J. Geosci.* **1993**, *6*, 32–45.
31. Heidarian, H.; Alirezaei, S.; Lentz, D.R. Chadormalu Kiruna-type magnetite-apatite deposit, Bafq district, Iran: Insights into hydrothermal alteration and petrogenesis from geochemical, fluid inclusion, and sulfur isotope data. *Ore Geol. Rev.* **2017**, *83*, 43–62.
32. Huckriede, R.; Kürsten, M.; Venzlaff, H. *Geotektonische Kartenskizze des Gebietes Zwischen Kerman und Sagand*, (*Iran*); Beih. Geol. Jb.: Honnover, Germany, 1962; 51, p. 197
33. NISCO. *Report on Results of Search and Evaluation Works at Magnetic Anomalies of the Bafq Iron Ore Region during 1976–1979*; NISCO: Tehran, Iran, 1980; Unpublished Internal Report.
34. Stosch, H.-G.; Romer, R.L.; Daliran, F.; Rhede, D. Uranium-lead ages of apatite from iron oxide ores of the Bafq district, east-central Iran. *Miner. Depos*. **2011**, *46*, 9–21.
35. Torab, F.; Lehmann, B. Magnetite-apatite deposits of the Bafq district, central Iran: Apatite geochemistry and monazite geochronology. *Mineral. Mag*. **2007**, *71*, 347–363.
36. Bonyadi, Z.; Davidson, G.J.; Mehrabi, B.; Meffre, S.; Ghazban, F. Significance of apatite REE depletion and monazite inclusions in the brecciated Se-Chahun iron oxide-apatite deposit, Bafq district, Iran: Insights from paragenesis and geochemistry. *Chem. Geol.* **2011**, *281*, 253–269.
37. Sabet-Mobarhan-Talab, A.; Alinia, F.; Asadi, F. Hydrothermal overprint of the Chador-Malu Kiruna-type deposit (Bafq district, central Iran) and associated REE mobilization: Evidence from mineralogy and geochemistry. *Iran. J. Econ. Environ. Sci*. **2014**, *5*, 1–14.
38. Sabet-Mobarhan-Talab, A.; Alinia, F. Mineralogy of the Chador-Malu iron ore deposit: Tracking the effects of hydrothermal overprinting. In Proceedings of the Conference on Mining Science, Islamic Azad University-Sari Branch, Sari, Iran, 2014.
39. Torab, F. Geochemistry and Metallogeny of Magnettite-Apatite Deposits of the Bafq Mining District, Central Iran. Ph.D. Thesis, Faculty of Energy and Economic Sciences, Technical University of Claustal, Clausthal, Germany, 2008; p. 131.
40. Jafarzadeh, A. *Die Magnetiterzlagerstätte Chador-Malu in Zentral Iran und Ihre Exploration*; Rheinisch-Westfälische Technische Hochschule Aachen: Aachen, Germany, 1981.
41. Förster, H.; Jafarzadeh, A. The Chador Malu iron ore deposit, Bafq district, central Iran, magnetite filled pipes. *Neues Jahrb. Geol. Paläontol. Abh*. **1984**, *168*, 524–534.
42. Zeng, L.-P.; Zhao, X.-F.; Li, X.-C.; Hu, H.; McFarlane, C. In situ elemental and isotopic analysis of fluorapatite from the Taocun magnetite-apatite deposit, eastern China: Constraints on fluid metasomatism. *Am. Mineral*. **2016**, *101*, 2468–2483.
43. Thomson, S.N.; Gehrels, G.E.; Ruiz, J.; Buchwaldt, R. Routine low-damage apatite U-Pb dating using laser ablation-multicollector-ICP MS. *Geochem. Geophys. Geosyst*. **2012**, *13*, 1-23.
44. Chew, D.M.; Petrus, J.A.; Kamber, B.S. U-Pb LA-ICP-MS dating using accessory mineral standards with variable common Pb. *Chem. Geol.* **2014**, *363*, 185–199.
45. Paton, C. Improved laser ablation U-Pb zircon geochronology through robust downhole fractionation correction. *Geochem. Geophys. Geosyst.* **2010**, *11*, 1–36.
46. Ludwig, K.R. (Ed.) *User's Manual for Isoplot 3.00*: *A Geochronological Toolkit for Microsoft Excel*; Berkeley geochronology center, Special Publication: Berkeley, CA, USA, 2003; p. 74.

47. Kani Kavan Sharq, *Geological Report and Genesis of Chadormalu Iron Ore Deposit* (*in Persian*); 2003; Unpublished Internal Report: Yazd, Iran, 2003.
48. Sepehrirad, R.; Alirezaei, S.; Azimzadeh, M. Hydrothermal alteration in the Gazestan iron ore deposit; comparison to other Kiruna-type iron deposits in central Iran. In Proceedings of the 35th National Geoscience Conference: Tehran, Iran, 25–27 February 2017.
49. Treloar, P.J.; Colley, H. Variations in F and Cl contents in apatites from magnetite-apatite ores in northern Chile, and their ore-genetic implications. *Mineral. Mag*. **1996**, *60*, 285–301.
50. Piccoli, P.M.; Candela, P.A. Apatite in igneous systems. *Rev. Mineral. Geochem*. **2002**, *48*, 255–292.
51. Moore, F.; Modabberi, S. Origin of Choghart iron oxide deposit, Bafq mining district, central Iran: New isotopic and geochemical evidence. *J. Sci. Islam. Repub. Iran* **2003**, *14*, 259–270.
52. Taghipour, S.; Kananian, A.; Harlov, D.; Oberhänsli, R. Kiruna-type iron oxide-apatite deposits, Bafq district, central Iran: Fluid-aided genesis of fluorapatite-monazite-xenotime assemblages. *Can. Mineral*. **2015**, *53*, 479–496.
53. Harlov, D.E.; Andersson, U.B.; Förster, H.-J.; Nyström, J.O.; Dulski, P.; Broman, C. Apatite-monazite relations in the Kiirunavaara magnetite-apatite ore, northern Sweden. *Chem. Geol.* **2002**, *191*, 47–72.
54. Belousova, E.; Griffin, W.; O'Reilly, S.Y.; Fisher, N. Apatite as an indicator mineral for mineral exploration: Trace-element compositions and their relationship to host rock type. *J. Geochem. Explor*. **2002**, *76*, 45–69.
55. Mao, M.; Rukhlov, A.S.; Rowins, S.M.; Spence, J.; Coogan, L.A. Apatite trace element compositions: A robust new tool for mineral exploration. *Econ. Geol.* **2016**, *111*, 1187–1222.
56. Anders, E.; Grevesse, N. Abundances of the elements: Meteoritic and solar. *Geochim. Cosmochim. Acta* **1989**, *53*, 197–214.
57. Hildebrand, R.S. Kiruna-type deposits; their origin and relationship to intermediate subvolcanic plutons in the great bear magmatic zone, northwest Canada. *Econ. Geol.* **1986**, *81*, 640–659.
58. Nystroem, J.O.; Henriquez, F. Magmatic features of iron ores of the Kiruna type in Chile and Sweden; ore textures and magnetite geochemistry. *Econ. Geol*. **1994**, *89*, 820–839.
59. Förster, H.-J.; Harlov, D. Monazite-(Ce)-huttonite solid solutions in granulite-facies metabasites from the Ivrea-Verbano zone, Italy. *Mineral. Mag.* **1999**, *63*, 587–587.
60. Ziemann, M.A.; Förster, H.-J.; Harlov, D.E.; Dirk, F. Origin of fluorapatite-monazite assemblages in a metamorphosed, sillimanite-bearing pegmatoid, Reinbolt Hills, east Antarctica. *Eur. J. Mineral*. **2005**, *17*, 567–579.
61. Hansen, E.C.; Harlov, D.E. Whole-rock, phosphate, and silicate compositional trends across an amphibolite- to granulite-facies transition, Tamil Nadu, India. *J. Petrol.* **2007**, *48*, 1641–1680.
62. Putnis, A. Mineral replacement reactions. In *Reviews in Mineralogy and Geochemistry, Thermodynamics and Kinetics of Water-Rock Interaction*; Oelkers, E.H., Schott, J., Eds.; Mineralogical society of America, Geochemical society: Chantilly, VA, USA, 2009; Volume 70, pp. 87–124.
63. Harlov, D.E.; Johansson, L.; Van Den Kerkhof, A.; Förster, H.-J. The role of advective fluid flow and diffusion during localized, solid-state dehydration: Söndrum Stenhuggeriet, Halmstad, SW Sweden. *J. Petrol.* **2005**, *47*, 3–33.
64. Boudreau, A.; McCallum, I. Low temperature alteration of REE-rich chlorapatite from the Stillwater complex, Montana. *Am. Mineral.* **1990**, *75*, 687–693.
65. Harlov, D.E.; Wirth, R.; Förster, H.-J. An experimental study of dissolution-reprecipitation in fluorapatite: Fluid infiltration and the formation of monazite. *Contrib. Mineral. Petrol*. **2005**, *150*, 268–286.
66. Jonsson, E.; Troll, V.R.; Högdahl, K.; Harris, C.; Weis, F.; Nilsson, K.P.; Skelton, A. Magmatic origin of giant 'Kiruna-type' apatite-iron-oxide ores in central Sweden. *Sci. Rep*. **2013**, *3*, 1644.
67. Knipping, J.L.; Bilenker, L.D.; Simon, A.C.; Reich, M.; Barra, F.; Deditius, A.P.; Lundstrom, C.; Bindeman, I.; Munizaga, R. Giant Kiruna-type deposits form by efficient flotation of magmatic magnetite suspensions. *Geology* **2015**, *43*, 591–594.
68. Bookstrom, A.A. The magnetite deposits of El Romeral, Chile. *Econ. Geol.* **1977**, *72*, 1101–1130.
69. Sillitoe, R.H.; Burrows, D.R. New field evidence bearing on the origin of the El Laco magnetite deposit, northern Chile. *Econ. Geol.* **2002**, *97*, 1101–1109.
70. Sarah, A.; Dare, S.; Barnes, S.-J.; Beaudoin, G. Did the massive magnetite "lava flows" of El Laco (Chile) form by magmatic or hydrothermal processes? New constraints from magnetite composition by LA-ICP-MS. *Miner. Depos.* **2015**, *50*, 607–617.

71. Parak, T. Kiruna iron ores are not "intrusive-magmatic ores of the Kiruna type". *Econ. Geol.* **1975**, *70*, 1242–1258.
72. Parak, T. On the magmatic origin of iron ores of the Kiruna type; discussion. *Econ. Geol.* **1984**, *79*, 1945–1949.
73. Mokhtari, M.A.A.; Zadeh, G.H.; Emami, M.H. Genesis of iron-apatite ores in Posht-e-Badam block (central Iran) using REE geochemistry. *J. Earth Syst. Sci.* **2013**, *122*, 795–807.
74. Mokhtari, M.A.A. Posht-e-Badam metallogenic block (central Iran): A suitable zone for REE mineralization. *Cent. Eur. Geol.* **2015**, *58*, 199–216.
75. Taghipour, S.; Kananian, A.; Somarin, A.K. Mineral chemistry and alteration parageneses of the Chogart iron oxide-apatite occurrence, Bafq district, central Iran. *Neues Jahrb. Geol. Paläontol. Abh*. **2013**, *269*, 221–240.
76. Mohseni, S.; Aftabi, A. Structural, textural, geochemical and isotopic signatures of synglaciogenic Neoproterozoic banded iron formations (BIFs) at Bafq mining district (BMD), central Iran: The possible Ediacaran missing link of BIFs in Tethyan metallogeny. *Ore Geol. Rev.* **2015**, *71*, 215–236.
77. Haas, J.R.; Shock, E.L.; Sassani, D.C. Rare earth elements in hydrothermal systems: Estimates of standard partial molal thermodynamic properties of aqueous complexes of the rare earth elements at high pressures and temperatures. *Geochim. Cosmochim. Acta* **1995**, *59*, 4329–4350.
78. Antignano, A.; Manning, C.E. Fluorapatite solubility in H_2O and H_2O–NaCl at 700 to 900 °C and 0.7 to 2.0 GPa. *Chem. Geol.* **2008**, *251*, 112–119.
79. Broman, C.; Nyström, J.O.; Henríquez, F.; Elfman, M. Fluid inclusions in magnetite-apatite ore from a cooling magmatic system at El Laco, Chile. *Gff* **1999**, *121*, 253–267.
80. Heidarian, H.; Alirezaei, S.; Lentz, D.R. *Apatite Chemistry from Kiruna-Type Bafq Iron Deposits, Central Iran: A Review*; SGA Abstract volume: Quebec, QC, Canada, 2017.
81. Marchig, V.; Gundlach, H.; Möller, P.; Schley, F. Some geochemical indicators for discrimination between diagenetic and hydrothermal metalliferous sediments. *Mar. Geol.* **1982**, *50*, 241–256.
82. Douville, E.; Bienvenu, P.; Charlou, J.L.; Donval, J.P.; Fouquet, Y.; Appriou, P.; Gamo, T. Yttrium and rare earth elements in fluids from various deep-sea hydrothermal systems. *Geochim. Cosmochim. Acta* **1999**, *63*, 627–643.
83. Knipping, J.L.; Bilenker, L.D.; Simon, A.C.; Reich, M.; Barra, F.; Deditius, A.P.; Wälle, M.; Heinrich, C.A.; Holtz, F.; Munizaga, R. Trace elements in magnetite from massive iron oxide-apatite deposits indicate a combined formation by igneous and magmatic-hydrothermal processes. *Geochim. Cosmochim. Acta* **2015**, *171*, 15–38.
84. Li, X.; Zhou, M.-F. Multiple stages of hydrothermal REE remobilization recorded in fluorapatite in the Paleoproterozoic Yinachang Fe–Cu–(REE) deposit, Southwest China. *Geochim. Cosmochim. Acta* **2015**, *166*, 53–73.
85. Alirezaei, S. Ore deposits and mineral resources of Iran: Temporal-spatial distribution and key targets. In *Trans-Disciplinary Research on Iranian Geology, Geodynamics, Earthquakes and Resources*; Agard, P., Ed.; Geological Survey of Iran: Tehran, Iran, 2017.
86. Heidarian, H.; Lentz, D.R.; Alirezaei, S. *An Overview of Iron Oxide-Apatite Deposits in the Bafq District, Central Iran*; Resources for Future Generations (RFG): Vancouver, BC, Canada, 2018.